

Swarmalators with delayed interactions

Nicholas Blum¹, Andre Li², Kevin O’Keeffe^{3,*} and Oleg Kogan^{1,†}

¹California Polytechnic State University, San Luis Obispo, California 93407, USA

²Department of Physics, California State University, East Bay, California 94542, USA

³Senseable City Lab, Massachusetts Institute of Technology, Cambridge, Massachusetts 02139, USA

 (Received 1 December 2022; revised 11 August 2023; accepted 15 September 2023; published 4 January 2024)

We investigate the effects of delayed interactions in a population of “swarmalators,” generalizations of phase oscillators that both synchronize in time and swarm through space. We discover two steady collective states: a state in which swarmalators are essentially motionless in a disk arranged in a pseudocrystalline order, and a boiling state in which the swarmalators again form a disk, but now the swarmalators near the boundary perform boiling-like convective motions. These states are reminiscent of the beating clusters seen in photoactivated colloids and the living crystals of starfish embryos.

DOI: [10.1103/PhysRevE.109.014205](https://doi.org/10.1103/PhysRevE.109.014205)

I. INTRODUCTION

Swarmalators are generalizations of phase oscillators that swarm around in space as they synchronize in time [1]. They are intended as prototypes for the many systems in which synchronization and swarming co-occur and interact, such as biological microswimmers [2–8], forced colloids [9–16], magnetic domain walls [17,18], robotic swarms [19–26], and embryonic cells of starfish [27] and zebrafish [28].

Research on swarmalators is increasing. Tanaka *et al.* began the endeavor by introducing a universal model of chemotactic oscillators with rich dynamics [29–32]. Later O’Keeffe *et al.* studied a mobile generalization of the Kuramoto model [1]. This swarmalator model is currently being further studied. The effects of phase noise [33], local coupling [21,34–36], external forcing [37], geometric confinement [38–40], pinning [41], mixed sign interactions [42–44], and finite population sizes [45] have been studied. The well posedness of weak and strong solutions to swarmalator models have also been addressed [46–48]. Reviews and potential application of swarmalators are provided in [49,50]. Mobile oscillators, where oscillators’ movements affect their phases but not conversely, have also been studied [51–54].

This paper is about swarmalators with delayed interactions. Delays are, in this context, largely unstudied, although they occur commonly in nature and technology. In the case of microswimmers, the interswimmer coupling is mediated by the surrounding fluid and is therefore noninstantaneous. Delays are also an important factor to consider in embryonic development. They are a well-established feature of gene expression and are believed to play a key role in how cells, organs, and other agglomerations attain their shapes [28]. The authors of [28] on page 26 say the following: “Even though cell coupling is local, involving cells which are in direct contact, cells require some time to synthesize and transport the membrane ligands and receptors to their surface. Also, cells

need time to integrate received information to its internal gene expression dynamics, for example, by producing transcription factors. Each of these reaction processes takes a different time to be completed, and these times depend on cell type and cell state.” They continue on the following page: “This time delay might be relevant for cell coupling because what cells acquire at the present time is the information of surrounding cells some time ago. Thus, inherent delays in cell coupling are key to understanding information flow in biological tissues.” Time delay is also relevant to robotic swarms where digital communication comes with unavoidable lags and may affect both communication of the spatial or internal state of robots.

In short, delays are important for a broad class of swarmalators; in some cases delay affects the communication of internal state of particles, and in others it affects the communication of both the internal and spatial state. Here we aim to advance our understanding of delay-coupled swarmalators theoretically, so we will focus on delays in just the internal state of the original swarmalator model [1]. This model is a natural first case study because it captures the behaviors of many natural swarmalators [4,5,11] yet is simple enough to analyze.

II. SWARMALATORS WITH DELAY

We will introduce time delay into the swarmalator model proposed by O’Keeffe, Hong, and Strogatz (OHS) [1]. The equations describing the dynamics of such delayed swarmalators read¹

$$\dot{\mathbf{r}}_i = \mathbf{v}_i + \frac{1}{N} \sum_{j \neq i}^N \left[\frac{\mathbf{r}_j - \mathbf{r}_i}{|\mathbf{r}_j - \mathbf{r}_i|} (1 + J \cos[\theta_j(t - \tau) - \theta_i(t)]) - \frac{\mathbf{r}_j - \mathbf{r}_i}{|\mathbf{r}_j - \mathbf{r}_i|^2} \right], \quad (1)$$

$$\dot{\theta}_i = \omega_i + \frac{K}{N} \sum_{j \neq i}^N \frac{\sin[\theta_j(t - \tau) - \theta_i(t)]}{|\mathbf{r}_j - \mathbf{r}_i|}. \quad (2)$$

¹While [1] is using the notation \mathbf{x} for positions of particles, here it will be more convenient to use \mathbf{r} , because we will also need to refer to the particle radius r in the analysis.

*kevin.p.okeeffe@gmail.com

†Present address: Department of Physics, Queens College of CUNY; oleg.kogan@qc.cuny.edu

Here $\mathbf{r}_i = (x_i, y_i)$ is the coordinate vector of the i th particle, θ_i is the phase of the i th particle, and N is the number of particles. All the spatial coordinates are evaluated without delay, at time t . The first coupling term in Eq. (1) represents attraction: it causes the velocity of particle j to be directed towards particle i and vice versa. The parameter J controls the tendency of this attractive term to depend on internal phases; when $J = 0$ the attraction is independent of internal phases. In order for the first term to be attractive, $|J|$ must be less than 1. The attractive term has a magnitude that is independent of the particle separation, i.e., it represents an all-to-all attraction (which could also be called mean field attraction) that is commonly used. For example, the same is done with phases in the Kuramoto model.

The second coupling term in Eq. (1) is a short-range repulsion: it causes the velocity of particle i to be directed away from particle j , but this term decays away with distance. It is intended to prevent clumping of all particles at one point. The form of the model is motivated in [1].

Equation (2) describes dynamics of internal phases. If θ_j is lagging behind θ_i , the $i - j$ term in the sum contributes to the velocity of θ_i , which tends to bring θ_i closer to θ_j . In other words, oscillator j “pulls” the phase of oscillator i closer to it. This is the usual Kuramoto interaction. The parameter K is an overall scaling factor for the strength of phase attraction (positive K) or repulsion (negative K). Here the strength of the interaction depends on the distance: oscillators that are closer in physical space will experience a stronger tendency to align or counteralign their phases with their close neighbors. Thus, the picture is this: the phase dynamics affects the strength of spatial attraction, while the spatial position of particles affects the strength of phase interaction.

What we add in this work is the time delay in phase dependence. The particle i at time t responds to the phase of the particle j as it was at time τ ago, at time $t - \tau$. In this work, we add this effect only to the phase dynamics. Physically, the phase represents the internal state, for example, the phase of a gene expression cycle. Communication of such an internal variable often takes place via chemical signals, which is a type of interaction that is much slower than the interaction that communicates positions of objects in physical space [28].

We investigate the role of delay in this model. OHS discovered that the system can be found in one of the five collective states in the absence of a delay. In the present paper we work mostly in the region of (J, K) space that in this delay-free model corresponds to what OHS called the “active phase wave.” The swarms in this state move in circles around the center of the annulus-shaped cluster: some move clockwise, and some counterclockwise, while the internal phases change as they move around the center of the annulus. It is in this region of the (J, K) space that we found the interesting collective behavior induced by a delay. It is possible that other unique behaviors take place in other regions of (J, K) space, but this would be a subject for a future work.

This plan of this paper is as follows. In Sec. III numerical results are presented. Two collective states are presented in Secs. III A and III B. Section III C describes the dynamical phase transition between these states, as well as properties of long-time behavior of transient oscillations. Theoretical treatment is presented Sec. IV, in which we compare

theoretical predictions with numerical results. We summarize in Sec. V.

III. TWO TYPES OF COLLECTIVE BEHAVIOR: NUMERICAL RESULTS

We begin by presenting a phenomenon that occurs at sufficiently large τ . The meaning of “sufficiently large” will be made precise in Sec. III C.

A. Quasistatic pseudocrystal

We placed particles at random positions \mathbf{x} within a square with corners at $(\pm 1, \pm 1)$ and assigned initial phases θ uniformly at random from $[0, 2\pi]$. The square refers to the set of initial positions, not the boundary conditions. The boundary conditions are free; the particles are not confined to a square. Following an initial complicated transient, when particles quickly organize into a nearly circular disk, the cluster enters into a coherent, synchronized collective motion characterized by decaying oscillations of the radius. Figure 1 demonstrates velocity vectors of particles at two snapshots in time—one during expansion and another during contraction—and Fig. 2(a) demonstrates oscillations of the system average radius of the cluster, $\bar{R}(t) = \frac{1}{N} \sum_{n=1}^N r_n(t)$, where $r_n = |\mathbf{r}_n|$. Naturally, the system average velocity and the average speed of particles also exhibit oscillations. Figure 2(b) depicts the average speed $\overline{|v|}(t) = \frac{1}{N} \sum_{n=1}^N |v_n|(t)$. We will refer to this collective behavior as “breathing” of the cluster. Note that in the rest of the paper, the word “average” will refer to the system average, as above; when the need arises to discuss other types of averages (for example, time average), this will be stated explicitly.

Because the oscillations during the breathing decay, this stage of the system dynamics can be thought of as the longer portion of the transient. At earlier times, the transient is more complicated and does not result in breathing motion. The dynamics at much earlier times is complex. The first few breaths are also complicated: they are not purely radial and can be accompanied by other types of dynamics, including particle rearrangements and time-averaged expansion of the cluster (this is why the speed does not go to zero at maximum and minimum radius). Eventually, breathing motion becomes simpler: it consists of only radial oscillations around the infinite-time equilibrium radius value, and there are no particle rearrangements in this latter stage. In Fig. 2 this happens around $t = 80$.

After the breathing transient dies down, it appears that a static pseudocrystal is formed; the average radius \bar{R} appears to reach a final, fixed value \bar{R}^* (the $*$ signifies the limit as $t \rightarrow \infty$). Examples of these pseudocrystals are shown in Fig. 3 for three system sizes. We use the term “pseudocrystals” because the crystalline order is only local and approximate. Note that the radii of these pseudocrystals depend on N ; i.e., the radii of the three clusters in Fig. 3 are not equal (see Fig. 7), they have been scaled in Fig. 3. But the interparticle spacing relative to the cluster radius clearly decreases with larger N .

Plots, such as in Fig. 2, suggest that a cluster reaches a static state. However, a careful examination of the tail of $\overline{|v|}(t)$ demonstrates that there is some residual motion left. This is

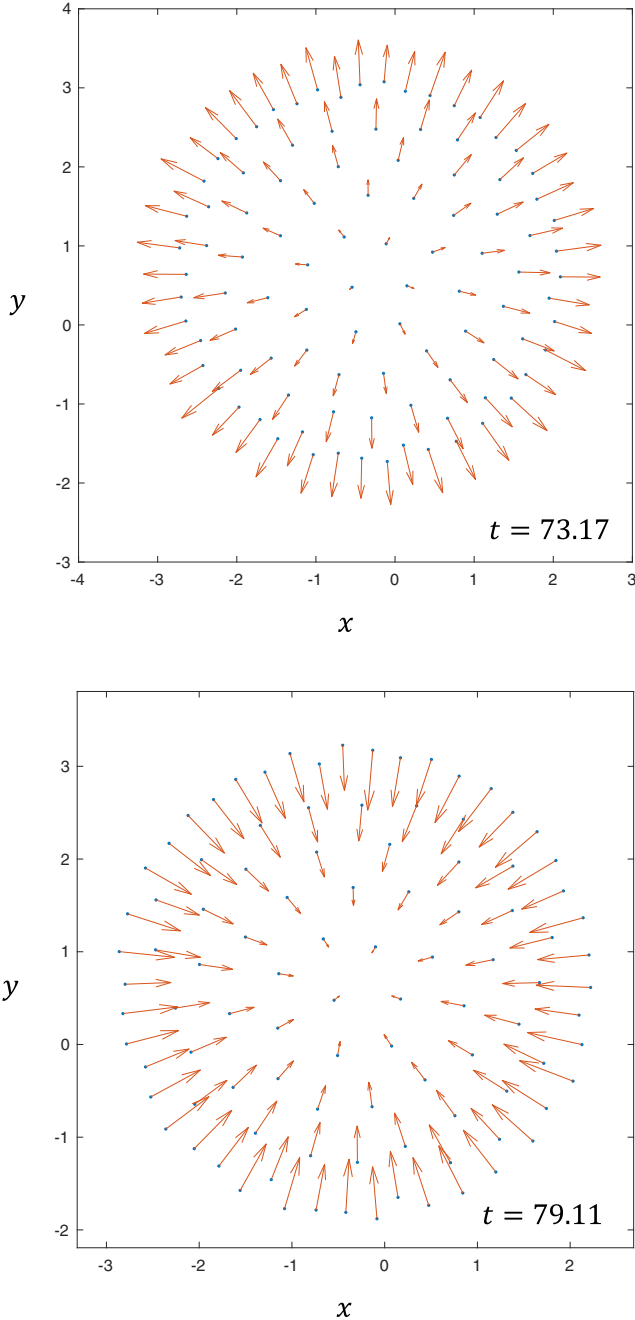


FIG. 1. Velocity vectors and particle positions at two instants of time. These times are at latter stages of oscillations (see Fig. 2 for corresponding speeds and the average radius (not maximum radius) at these times). $(N, J, K, \tau) = (100, 1, -0.75, 8)$.

seen on a log scale, such as in Fig. 4. Around $t = 150$ we clearly see that breathing motion gives way to a different type of motion with very small velocities. We can call it creeping motion. The magnitude of these velocities continues to decay with time, but much slower than during the breathing stage. We can define the transition to this creeping motion as an intersection of the straight-line fit on the logarithmic plot to the envelope of $|\bar{v}|(t)$ during breathing (red dashed line in Fig. 4) with the function itself. There is no single defining feature of this postbreathing velocity pattern: its character

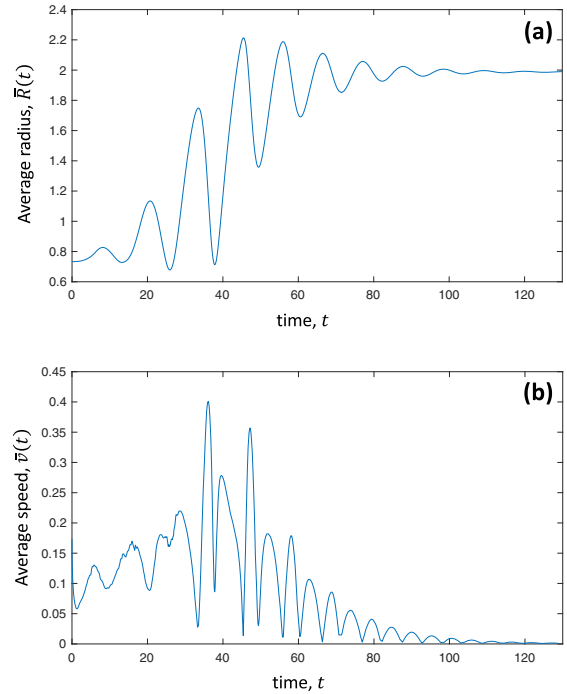


FIG. 2. (a) $\bar{R}(t)$; (b) $\bar{v}(t)$. The parameters are $(N, J, K, \tau) = (100, 1, -0.75, 8)$.

changes with time and with respect to parameters. The only definite feature of this postbreathing creeping dynamics is that it is rather disordered. We give an example of such a pattern in Fig. 5. Additional examples can be found in Figs. 29 and 30 in Appendix B.

There is no indication, given the range of our computational capabilities, that the postbreathing creeping motion is a finite-size effect. We come to this conclusion by measuring the dependence of the average speed on N at three instants of time that follow the breathing. In Fig. 6 we plot the average speed versus N measured at three instants in time. The first, labeled “time 1,” is immediately after the end of the breathing motion as just defined. The second, or “time 2,” is around 500 time units after end of the breathing motion, and the third, or “time 3,” is 1000 time units after the end of the breathing motion. The data in Fig. 6 suggest that there is no indication (at least in the range of N 's that were studied) that the long-time average speed decreases with increasing system size.

Other properties do exhibit N dependence, for example, the radius of the cluster after breathing (creeping motion has a negligible effect on cluster radius fluctuations). We will denote the radius of the cluster by R (no overbar means we refer to the radius of the cluster, i.e., the maximal r out of N particles, not the average over N values of r); thus, the infinite time limit of this quantity will be denoted by R^* . Figure 7 clearly demonstrates that R^* depends on N .

So far we have discussed the spatial aspect of the dynamics. Figure 8 depicts the dynamics of internal phases. We see again the early transient, the longer portion of the transient coincident with the breathing stage, followed by the long-time behavior of uniform growth of internal phases all at the same rate. During the longer stage of the transient the phases

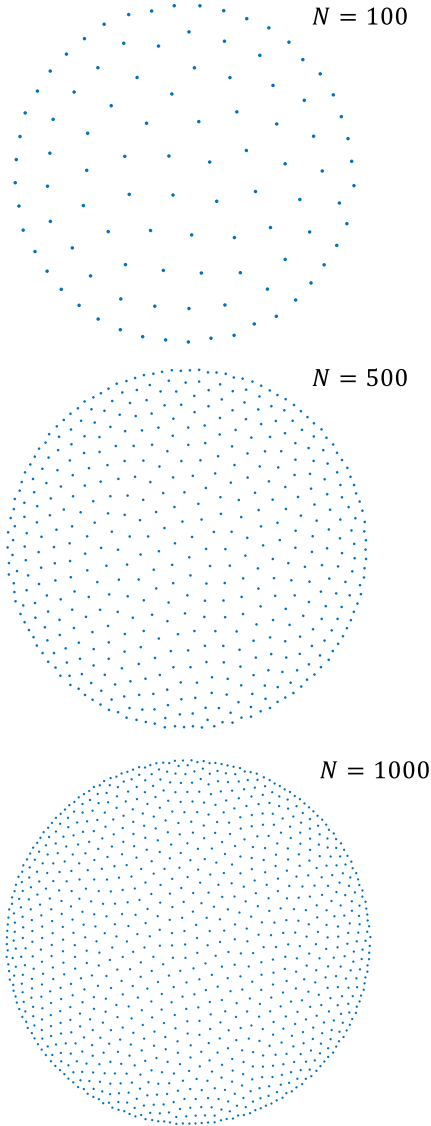


FIG. 3. $N = 100$ (top), $N = 500$ (middle) and $N = 1000$ (bottom) particle systems after the breathing transient. The values of τ were $1.5\tau_c$, where τ_c is a critical delay at which the long-time behavior becomes boiling motion, as described in the next subsection (see Fig. 16 for values of τ_c at different N). Here $J = 1$, $K = -0.7$.

undergo a series of plateaus followed by short and rapid collective phase slips. Note that at this time all the phases are either the same or separated by 2π . Therefore, there is not only a synchronization of spatial motion (coherent breathing) but also a phase synchronization. The behavior after the early transient can be expressed as $\theta = \Omega t + \delta\theta(t)$, where $\delta\theta(t)$ is an oscillatory function that decays away, leaving behind only the uniform growth of all phases after the transient. Note that the period of $\delta\theta(t)$ is comparable to τ . The Ω can be positive or negative, depending on initial condition.

A detailed example of the time evolution is shown in Fig. 31 in Appendix B. We also show the evolution of several quantities with increasing τ in Fig. 32 there, where it is evident that plateaus of $\theta(t)$ become more prominent and grow with increasing τ .

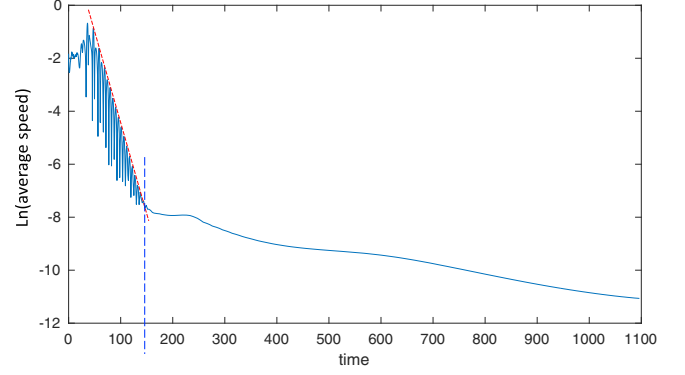


FIG. 4. Natural logarithm of the average speed versus time. A transition from decaying oscillatory motion to creeping motion is very clear. Here $(N, J, K, \tau) = (100, 1, -0.75, 8)$.

Before moving on to discuss the boiling collective state, we present data on $R^*(\tau)$ for two different values of N . This is demonstrated in Fig. 9, where R_c^* is the value of R^* at τ_c . Below τ_c the value of R^* becomes less well defined, since it is no longer a static surface, as we will see in the next section. Note the collapse of the data in Fig. 9(b) onto one universal curve when plotting the dimensionless deviation of the radius $(R^* - R_c^*)/R_c^*$ vs the dimensionless deviation of the delay $(\tau - \tau_c)/\tau_c$.

B. The boiling state

At smaller delays, the long breathing part of the transient gives way to a dynamic state, rather than a quasistatic crystal. In this collective state, swarmalators at the surface of the cluster undergo convective-like motion, while the swarmalators deeper in the interior are essentially frozen, similar to

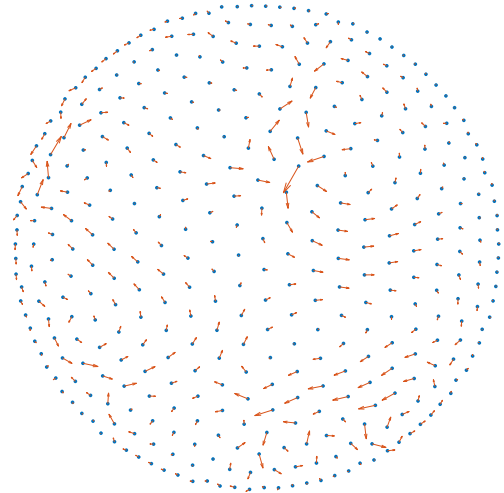


FIG. 5. Creeping particle motion for $t \approx 5000$, which is approximately 10 times the time at which the breathing ceased, as defined above. Here $N = 400$, and the values of τ are $1.5\tau_c$ (see Fig. 16 for values of τ_c), $J = 1$, and $K = -0.7$. The vectors have been automatically rescaled to be visible. Thus, while the arrows appear to have the length comparable to those in Fig. 1, this is because of the up-scaling.

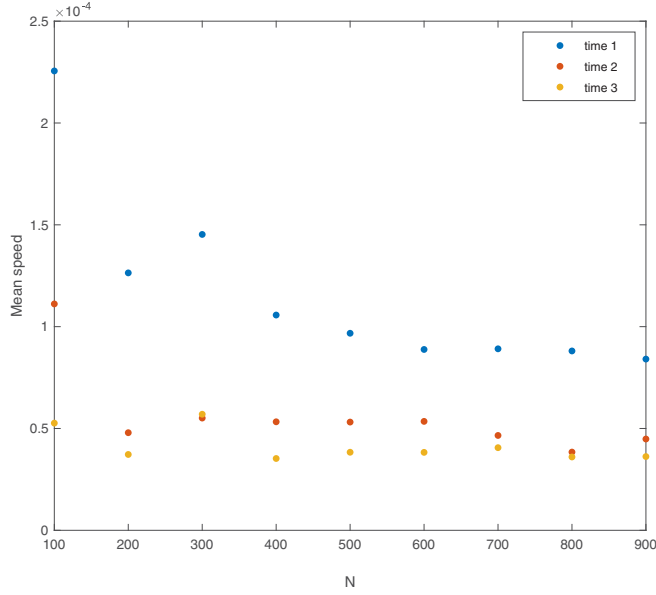


FIG. 6. Dependence of creeping velocity on the system size. Time 1 is immediately after the end of the breathing motion, time 2 around 500 time units after the end of the breathing motion, and time 3 around 1000 time units after the end of the breathing motion. The τ value was chosen to be $1.5\tau_c$ (see Sec. III C and Fig. 16 for discussion of τ_c). Here $(J, K) = (1, -0.7)$.

the quasistatic situation in the previous subsection. For this reason, we called it the boiling state, as it looks like the surface of the cluster is boiling. Figure 10 demonstrates two snapshots of a cluster in such a boiling state. We again look at the time evolution of the average radius and average speed (Fig. 11). In contrast to the lower τ situation, the residual velocity after the breathing now comes from the swarmalators in the boiling layer near the surface. The type of motion in the boiling state

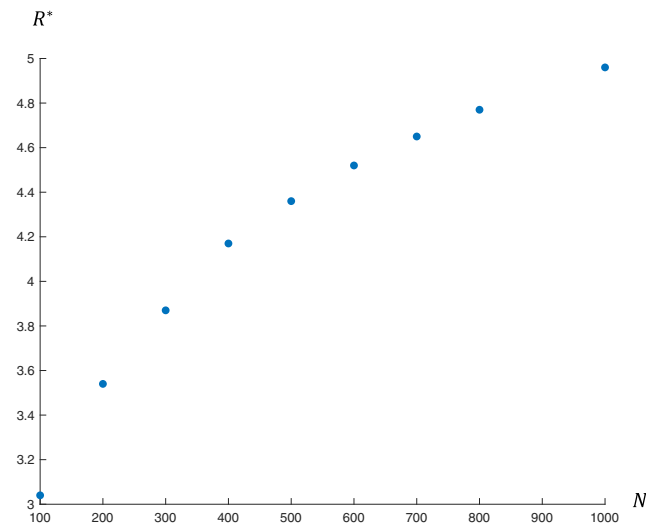


FIG. 7. Cluster radius dependence on N (the effect of creeping motion is negligible, so the cluster can be considered static, with a well-defined radius). The τ value is chosen to be $1.5\tau_c$ (see Sec. III C and Fig. 16 for discussion of τ_c). Here $(J, K, \tau) = (1, -0.7)$.

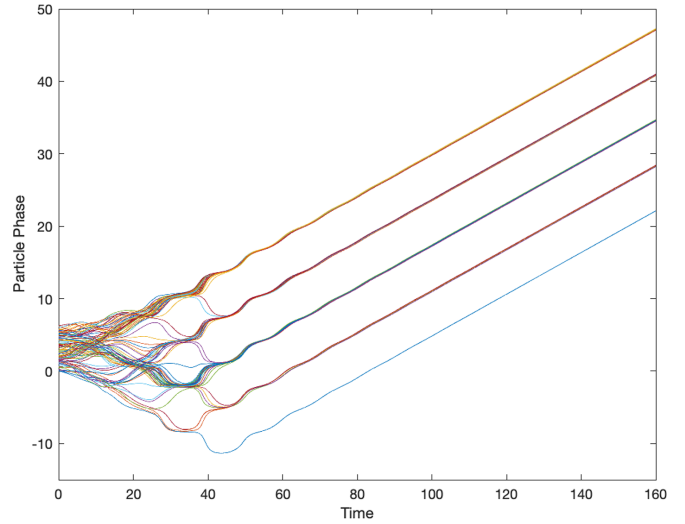


FIG. 8. Dynamics of internal phases. The different groups are separated by 2π . Here $(N, J, K, \tau) = (100, 1, -0.75, 8)$.

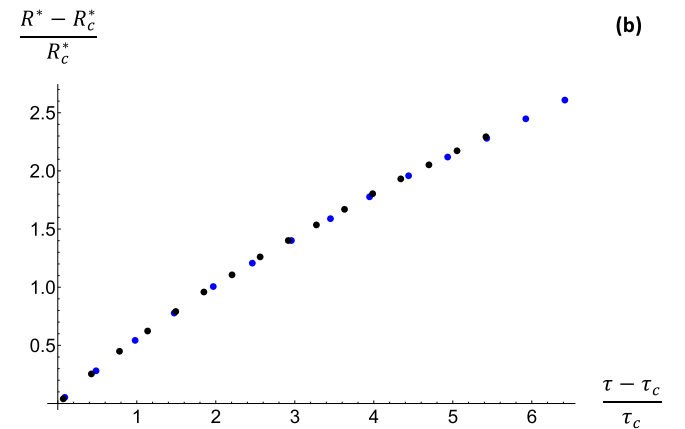
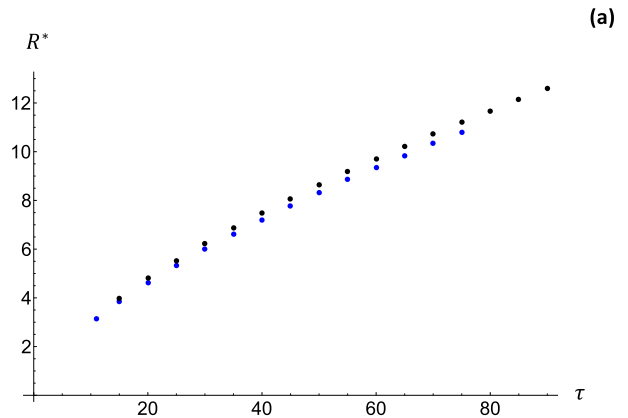


FIG. 9. (a) $R^*(\tau)$ for two values of N . Top (black) is for $N = 1000$ and bottom (blue) is for $N = 300$. The values for τ_c are ≈ 14 and ≈ 10.1 for respective system sizes (see Fig. 16). Here $J = 1$, and $K = -0.7$. (b) The data are plotted versus a rescaled variable. The data collapse is evident. The error bars are not shown because they are very small for this value of parameters.

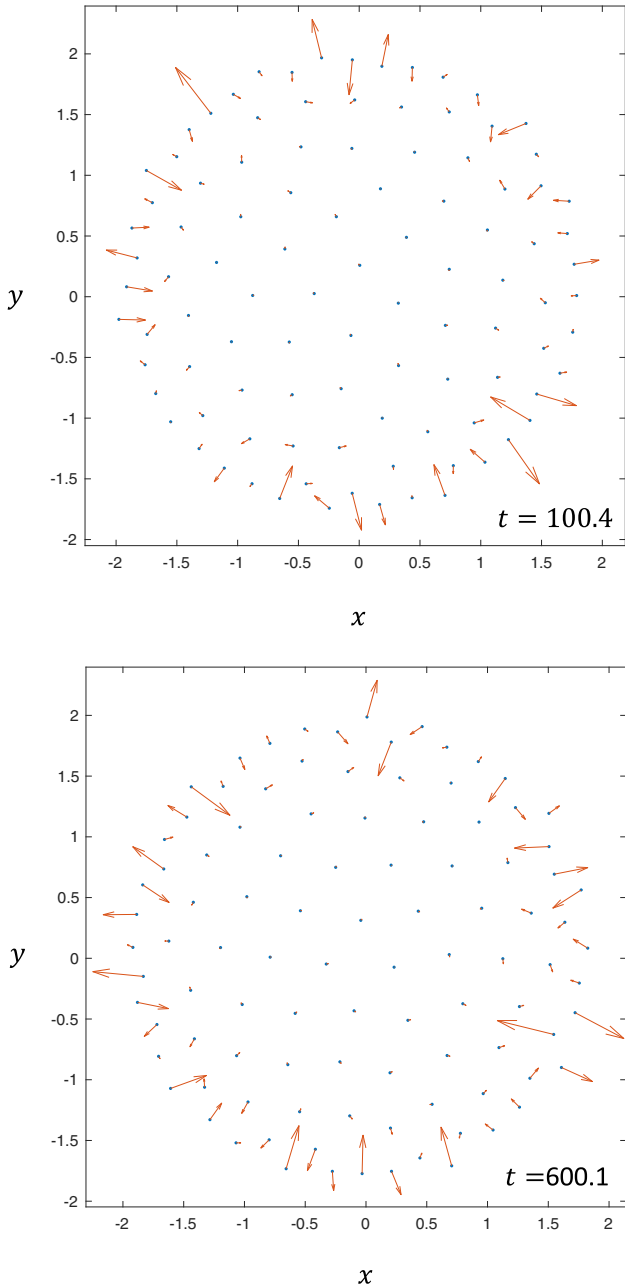


FIG. 10. Velocity vector plots at two instants of time for the boiling state. The parameters are $(N, J, K, \tau) = (100, 1, -0.75, 5)$.

is qualitatively different from the creeping motion, and the value of the average velocity is also larger by at least an order of magnitude. The dynamics of internal phases is similar to the the phase dynamics in the higher τ collective state (Fig. 12).

C. Delay-induced transition

We presented two types of collective states that develop after the breathing transient: the pseudocrystalline phase at larger delay, and the boiling state at smaller delay. We will now discuss the transition between these states and make more precise the meaning of “larger” or “smaller” delay. Consider

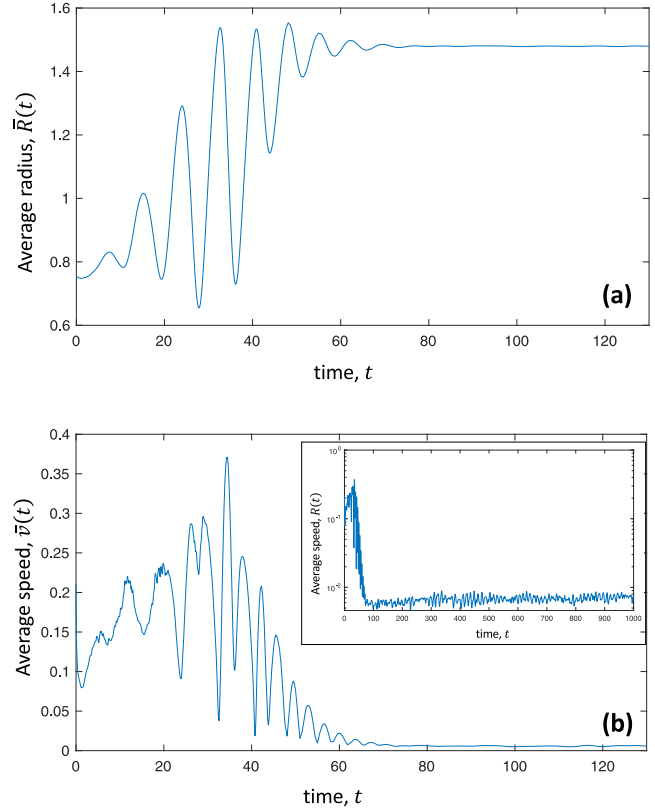


FIG. 11. (a) $\bar{R}(t)$; (b) $\bar{v}(t)$. The parameters are $(N, J, K, \tau) = (100, 1, -0.75, 5)$.

the plot of the average speed versus τ in Fig. 13, collected at $t = 1500$. Note that for all τ presented in this figure, $t = 1500$ is considerably after the breathing has given way to either the quasistatic pseudocrystal or boiling, as described above. For example, this transition takes place at $t \approx 80$ for $\tau = 5$, at $t \approx 150$ for $\tau = 8$, and at $t \approx 250$ for $\tau = 11$. For this reason, the y axis of Fig. 13 is called “Average speed long after breathing.” Aside from fluctuations in the boiling regime and

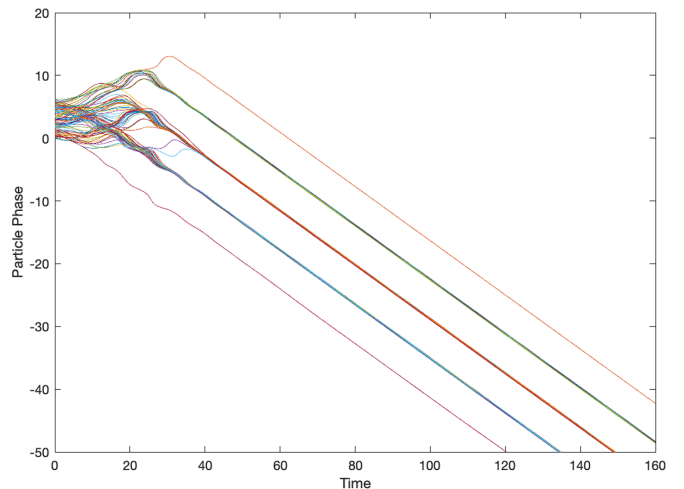


FIG. 12. Dynamics of internal phases. The different groups are separated by 2π . Here $(N, J, K, \tau) = (100, 1, -0.75, 5)$.

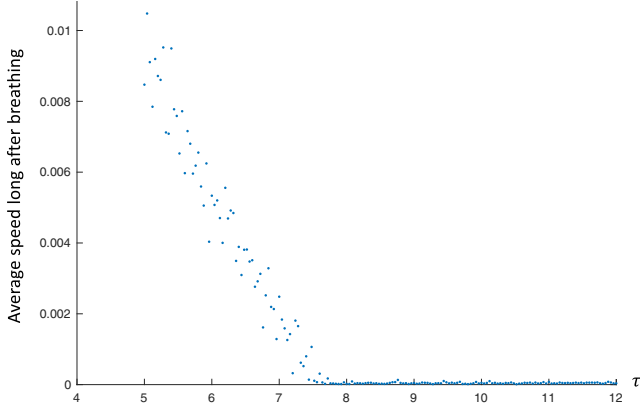


FIG. 13. Average speed collected at $t = 1500$ after the initial condition. The parameters are $(N, J, K) = (100, 1, -0.7)$.

in the absence of creeping motion in the quasistatic regime, this would have been called “Average speed at infinite times.”

There is a well-defined transition at a certain τ , which we will call τ_c . It corresponds to the transition between the boiling state at smaller τ and the quasistatic state at larger τ . Another obvious feature of Fig. 13 are fluctuations in the average velocity below τ_c . We found that time averaging the velocity (in addition to system average) does not get rid of these fluctuations. Therefore, we believe that these fluctuations result from different initial conditions from one simulation to the next. Moreover, setting identical (up to machine precision) initial particle positions and internal phases still gives rise to these types of fluctuations. We hypothesize that this is similar, or perhaps identical, to chaotic divergence, since a different parameter (here, τ) will result in different trajectories $\mathbf{x}_i(t)$ and $\theta_i(t)$ between even very nearby τ .

The critical τ can be extracted by fitting the lower- τ portion of the graph by a straight line and extracting the τ of the x intercept. Figure 14 presents τ_c thus extracted from numerical

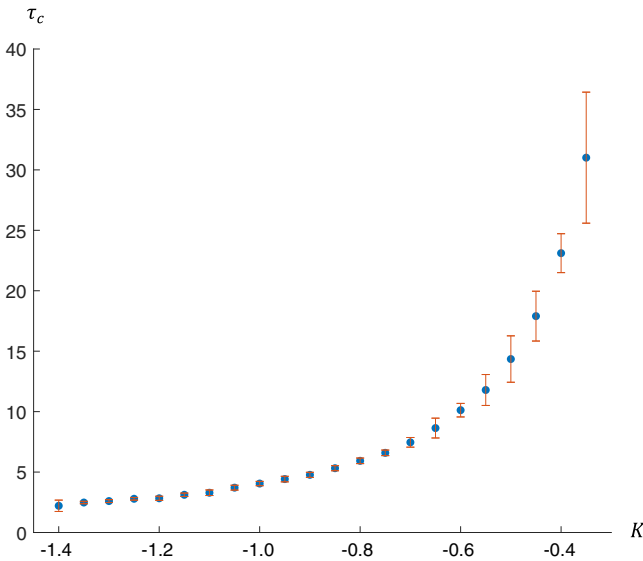


FIG. 14. Dependence of the critical delay on K . The other parameters are $(N, J) = (100, 1)$.

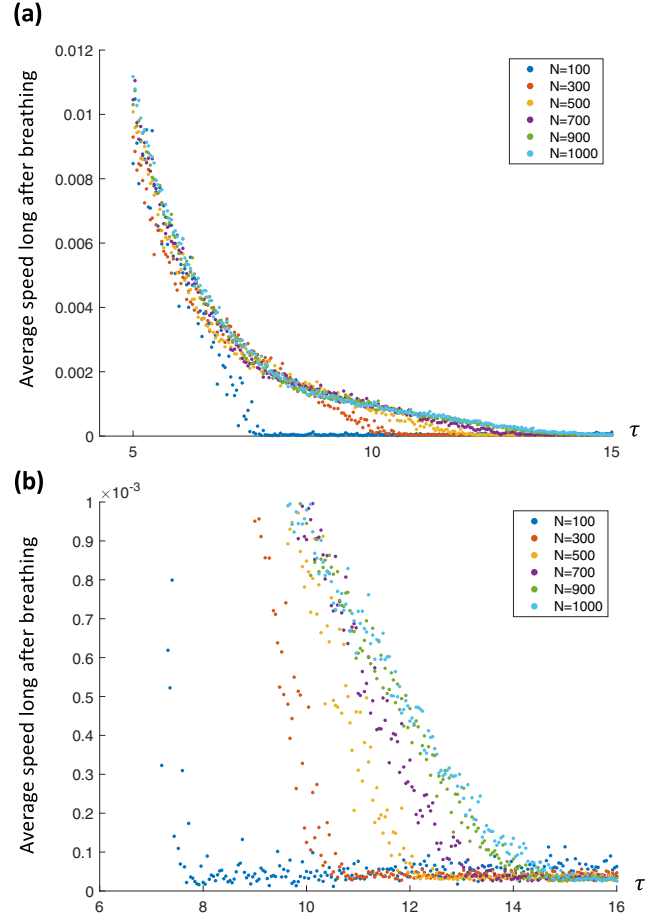


FIG. 15. (a) Average speed vs τ for several N , measured at $t = 1500$ after the initial condition. The parameter values are $(J, K) = (1, -0.7)$. For all parameters presented, $t = 1500$ is significantly greater than the time at which breathing gives way to either boiling or pseudocrystal. (b) Same data, zooming in on the range of the y axis to demonstrate the evolution of τ_c with increasing N . The values above τ_c do not reach all the way to zero because of the creeping motion after the breathing, as described above (the lowest values are $\sim 5 \times 10^{-5}$, which is comparable to what we see in Fig. 4).

calculations versus the coupling strength K at $J = 1$. The boiling regime lies below the curve. There appears to be a minimal value of $|K|$ below which it is impossible to induce a pseudocrystal, no matter the value of τ . As $|K|$ decreases, and approaches this minimal $|K|$, the fluctuations grow. Both of these observations remind us of critical phenomena.

We will now demonstrate how the transition from breathing to boiling depends on the system size. First, Fig. 15 is analogous to Fig. 13 but includes data on progressively larger system sizes. If we restrict the range of the y axis [Fig. 15(b)], it becomes clear that τ_c displays a trend towards a limiting value. This saturation is also evident in Fig. 16.

It is important to emphasize that oscillations persist below τ_c . Above τ_c , oscillations give way to the quasistatic pseudocrystal at large times. Below τ_c , oscillations give way to the boiling state at large times. Thus, τ_c delimits two large-time (or infinite time) behaviors after the breathing transient has

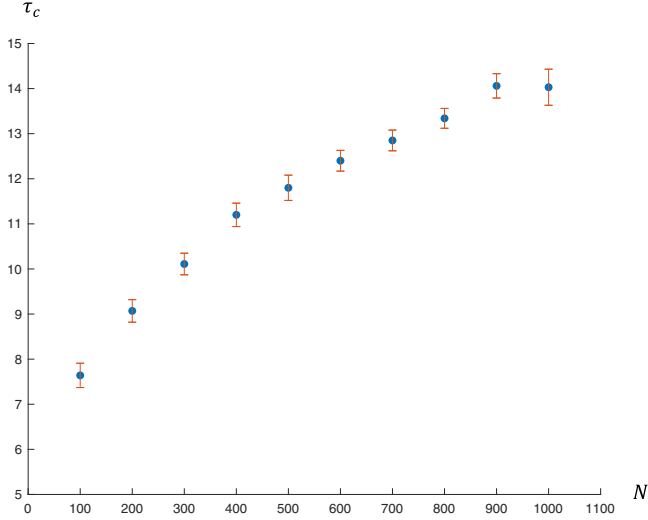


FIG. 16. Dependence of the critical delay on the system size. Here $(J, K) = (1, -0.70)$. The data were collected at $t = 1500$ after the initial condition.

subsided; it does not refer to properties of breathing oscillations. Figure 33 in Appendix B demonstrates the evolution of the average speed and the average radius across τ , from above τ_c to below τ_c . We see that as τ crosses below τ_c , the boiling layer begins to develop. As τ is progressively decreased, the thickness of the boiling layer grows. The long-time value of the average radius becomes less and less well defined, since the boiling of the surface leads to increasing fluctuations of this quantity. However, as long as the system is in the boiling regime, the phases synchronize.

At even lower values of τ , we would encounter another transition, τ_l , below which the phases no longer synchronize. In the region of (J, K) parameter space in which we have done numerical investigations, we found that in this lower τ regime the dynamical behavior resembles active phase waves. However, the situation in other regions of parameter space may be different; most of our numerical exploration took place in the (J, K) region that corresponds to the active phase waves in the absence of the delay.

Thus, the frequency ω and decay rates λ of breathing oscillations should smoothly vary across τ_c ; τ_c refers to the large-time behavior, not to properties of breathing oscillations. We present the numerical results for $\omega(\tau)$ and $\lambda(\tau)$ in Fig. 17.

We make two important remarks. First, note that in contrast to Fig. 9(a), the data for $N = 300$ and $N = 1000$ follow essentially the same functional dependence, so there is no need to rescale the variables to achieve data collapse; there is already a data collapse as is. Second, we see that this collapse is better for ω than for λ . One might also ask why the data were not collected at lower τ 's. In order to extract this pair of parameters (for example, ω and r), we have to fit the late-time tail of $R(t)$ data generated by the simulation to the functional form $Ae^{-\lambda t} \cos(\omega t + \phi) + B$; or, we have to subtract the B from the data first and then make the fit with zero B . In either case, we have to know the B from the long-time asymptote towards which $R(t)$ relaxes but sufficiently below τ_c , that the asymptote is noisy due to the fluctuations of the surfaces,

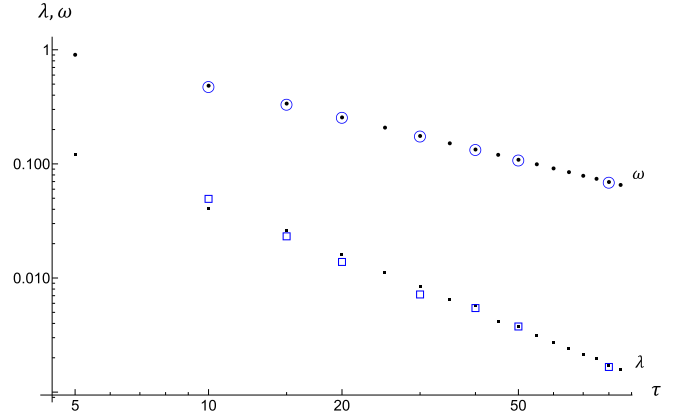


FIG. 17. Decay rates λ (squares) and angular frequencies ω (circles) of breathing oscillations obtained from numerical simulations. Blue open symbols, $N = 300$; black solid symbols, $N = 1000$.

as explained above. At the same time, the decay rate grows. Thus, these parameters estimated from such a fit become less and less accurate at lower τ . The theoretical approach laid out next misses fluctuations, so it allows us to predict $\lambda(\tau)$ and $\omega(\tau)$ down to lower values of τ .

D. Summary of phenomenology

Before proceeding to the theoretical calculations, we briefly summarize phenomenological findings and parameter scans performed. We described a long breathing transient. The important control parameter is the delay time τ . There exists a special value of $\tau = \tau_c$. For $\tau > \tau_c$, the breathing transient decays into quasistationary pseudocrystal. It is quasistationary because it is accompanied by creeping motion of particles. For $\tau < \tau_c$, the breathing transient decays into the boiling state, characterized by convective, boiling-like motion of particles at the surface. The average speed serves as the order parameter; for $\tau < \tau_c$ it grows linearly with $|\tau - \tau_c|$. We investigated the dependence of τ_c with K and found that $|K|$ has to be sufficiently large for τ_c to exist. We also investigated the dependence of τ_c with the system size N . We investigated the dependence of the radius of the quasistatic cluster on τ and N . Finally, we studied the scaling of the frequency and decay rates of breathing oscillations with τ .

IV. THEORETICAL UNDERSTANDING OF COLLECTIVE BREATHING

A. Self-consistent solution to density profiles

Our simulations revealed for τ that on both sides of τ_c the phase slips decay away at long times, and all phases advance uniformly with rate Ω . We also observed that this is accompanied by freezing out of spatial motion; i.e., all \mathbf{r}_i reach a constant value \mathbf{r}_i^* (aside from the creeping motion, which we will ignore for the theory). Therefore, at large times, Eq. (2) becomes

$$\Omega = -\sin(\Omega\tau) \frac{K}{N} \sum_{j \neq i} \frac{1}{|\mathbf{r}_j^* - \mathbf{r}_i^*|}. \quad (3)$$

Here the word “large” means $t \gg$ relaxation time, which will be calculated below. The sum is some constant number. On the one hand, it seems to depend on the position of this i th oscillator. On the other hand, it equals a constant that is independent of i , so this will translate to a self-consistency argument on the density of oscillators, which we will analyze below.

To calculate the sum, we will define $\rho(r)$ to be the equilibrium density of swarmalators (here $r = |\mathbf{r}|$), such that $\rho(r)r dr d\theta$ is the number of swarmalators in a differential area $r dr d\theta$. We have assumed a radial symmetry, which invites the use of polar variables and is the reason why ρ is a function of only the radius. This assumption conforms to our observations, and it is expected because there are no symmetry-breaking fields. With the help of this density, we can pass into the continuum limit. After some details that are relegated to Appendix A 1, Eq. (3) is transformed into

$$\Omega = -2 \sin(\Omega\tau) \frac{K}{N} \int_0^R dr \int_0^\pi \frac{\rho(r)r d\alpha}{\sqrt{r^2 + l^2 - 2rl \cos \alpha}}. \quad (4)$$

Here R is the radius of the whole cluster, and l is the radius of i th swarmalator. The integral over α evaluates to $\frac{2K[\frac{4lr}{(r+l)^2}]}{(r+l)}$, where K is a complete elliptic integral of the first kind. It diverges when its argument is 1, which will happen when $r = l$. We depict $K[\frac{4lr}{(r+l)^2}]$ vs r for several l in Fig. 26, also in Appendix A 1.

To continue further, we need to know $\rho(r)$, which is not given *a priori*. However, we can determine it self-consistently. Note that integrals are functions of l , the radius of the i th swarmalator. On the other hand, the left-hand side of Eq. (3) must be independent of l : it must be the same for all swarmalators. Therefore, $\rho(r)$ must be a special function that will ensure that the answer is independent of l . Before seeking this self-consistent solution, it helps to reason physically what we expect such a special $\rho(r)$ to be. Equation (3) is a sum of $1/\text{distance}$ between swarmalator i and all the other swarmalators j . In the vicinity of the center of the swarm, this sum is essentially invariant as we sample different i around this center. Closer to the edge, essentially a large part of the sum is missing; about a half of the swarm is missing. So, to compensate for this, ρ must increase towards the edge if we are to have the same value of the sum for all i .

We now seek $\rho(r)$ self-consistently. It is useful to define $\tilde{\rho}(r) = -\frac{4RK \sin(\Omega\tau)}{N\Omega} \rho(r)$, and further, to change variables $x = r/R$ and $L = l/R$. With all these changes, Eq. (4) becomes

$$1 = \int_0^1 x \tilde{\rho}(x) \frac{K[\frac{4Lx}{(x+L)^2}]}{(x+L)} dx = \int_0^1 \tilde{\rho}(x) \mathcal{K}(L, x) dx. \quad (5)$$

Our objective is to find such $\tilde{\rho}(x)$ that makes this true for any L . We do this numerically, by approximating the integral by a discrete sum, giving the following set of equations:

$$\begin{aligned} 1 &= [\tilde{\rho}(x_1)\mathcal{K}(L_1, x_1) + \tilde{\rho}(x_2)\mathcal{K}(L_1, x_2) + \dots \\ &\quad + \tilde{\rho}(x_n)\mathcal{K}(L_1, x_n)]\Delta x, \\ 1 &= [\tilde{\rho}(x_1)\mathcal{K}(L_2, x_1) + \tilde{\rho}(x_2)\mathcal{K}(L_2, x_2) + \dots \\ &\quad + \tilde{\rho}(x_n)\mathcal{K}(L_2, x_n)]\Delta x, \\ &\dots \end{aligned}$$

$$\begin{aligned} 1 &= [\tilde{\rho}(x_1)\mathcal{K}(L_n, x_1) + \tilde{\rho}(x_2)\mathcal{K}(L_n, x_2) + \dots \\ &\quad + \tilde{\rho}(x_n)\mathcal{K}(L_n, x_n)]\Delta x. \end{aligned} \quad (6)$$

We construct a matrix of kernels $\mathcal{K}(L_n, x_m)\Delta x$, then invert this matrix, operate on the vector $(1, 1, \dots, 1)$, and find a vector $(\tilde{\rho}(x_1), \tilde{\rho}(x_2), \dots, \tilde{\rho}(x_{n_{\max}}))$. Because \mathcal{K} diverges when its argument is 1, the same values could not be used for L 's and x 's. We choose $x_n = \frac{n}{n_{\max}}$ and $L_n = \frac{n}{n_{\max}} + 10^{-4}$, where n_{\max} is typically on the order of a thousand. The result of this calculation with $n_{\max} = 600$ is displayed in Fig. 18 in red. The function $\tilde{\rho}(x)$ is dimensionless and parameter-free - it describes the functional form of the density profile.

The density increases at the edge, as expected. The divergence at $x = 1$ appears to have an exponent very close to $1/2$, i.e., to have the form $(1-x)^{-1/2}$ close to $x = 1$. The function $\tilde{\rho}$ is not a pure power law over the entire domain $[0, 1]$. However, we would like to model this result by an analytical expression in order to make tractable, analytical predictions. We found that the function $0.3(1-x)^{-1/2}$ approximates the whole numerical result $\tilde{\rho}(x)$ very well; see Fig. 18. We checked that $0.3(1-x)^{-1/2}$ makes the integral $\int_0^1 \rho(x)\mathcal{K}(L, x) dx$ very nearly a constant with respect to L [keeping in mind that $0.3(1-x)^{-1/2}$ is an approximation]. The total number of swarmalators inside the cluster should be equal to N . Therefore

$$\begin{aligned} N &= 2\pi \int_0^R \rho(r)r dr = -2\pi \frac{N\Omega}{4RK \sin(\Omega\tau)} \int_0^R r \tilde{\rho}(r) dr \\ &= -\frac{N\pi\Omega}{2RK \sin(\Omega\tau)} R^2 \int_0^1 x \tilde{\rho}(x) dx \\ &\approx -\frac{NR\pi\Omega}{2K \sin(\Omega\tau)} \int_0^1 0.3x(1-x)^{-1/2} dx. \end{aligned}$$

Here $\tilde{\rho}(x)$ means $\tilde{\rho}(r(x))$. The integral evaluates to 0.4, so

$$\frac{\Omega}{\sin(\Omega\tau)} = -\frac{5K}{R\pi}. \quad (7)$$

Therefore,

$$\rho(r) = \frac{5}{4} \frac{N}{\pi R^2} \tilde{\rho}(r). \quad (8)$$

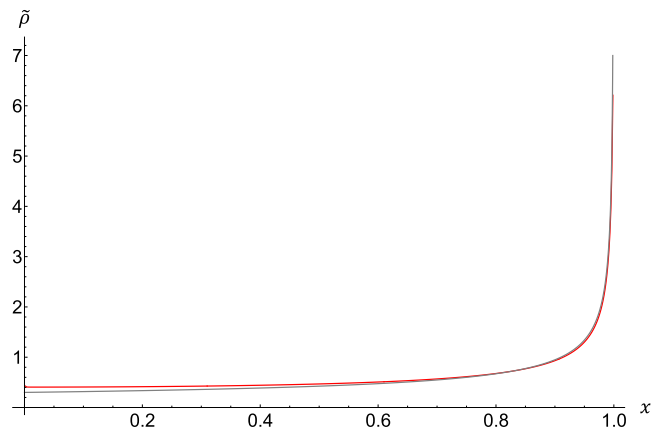


FIG. 18. Red (slightly higher curve at small x), $\tilde{\rho}$ obtained from the solution of Eq. (6); gray, $0.3(1-x)^{-1/2}$.

For example, if $\tilde{\rho}(x) = 0.3(1-x)^{-1/2}$, then $\rho(r) = \frac{3}{8} \frac{N}{\pi R^2} (1 - \frac{r}{R})^{-1/2}$. This $\rho(r)$ is normalized, i.e., $2\pi \int_0^R r \rho(r) dr = N$. The expression for ρ in Eq. (8) is not complete, because we do not know how R depends on N and other parameters. So we need more information in order to close this expression and make it self-contained. We will attempt to use the spatial equation for this purpose. The $\tilde{\rho}$ is a parameter-free, dimensionless function that is a solution to Eq. (5). We obtained it numerically by discretizing the radial variable and insisting that the integral in Eq. (5) should be independent of L and always gives 1.

The radial density function is $\mathcal{R}(r) = 2\pi r \rho(r) = \frac{5}{2} \frac{N}{R^2} r \tilde{\rho}(r)$. This is expressed as a function of r that goes between 0 and R . If we want to express it as a function of a dimensionless variable $x \equiv \frac{r}{R}$, that goes between 0 and 1, the answer is $\mathcal{R}(x) = \frac{5}{2} N x \tilde{\rho}(x)$ (see comment in Appendix A 2).

We now compare the density profile \mathcal{R} with the data from simulations. We performed ten simulations from $\tau = 17.0$ to $\tau = 17.9$ in increments of 0.1. For each value for τ , ten simulations were performed with $N = 1000$ particles.

The number of particles within each radius bin were counted [i.e., this will be approximated by $2\pi r \rho(r) \Delta r$, where $\rho(r)$ is the correct continuum radial density] and plotted versus the variable $x = r/R$. Results over ten simulations for each τ were averaged. The inset of Fig. 19 shows this average, one for each value of τ (dots). The data (dots) collapse onto one universal curve, as the theory suggests. Moreover, this curve closely matches the theoretical $\mathcal{R} = \frac{5}{2} N x \tilde{\rho}(x)$, shown as a red solid curve. The main part of Fig. 19 compares the theoretical $\mathcal{R}(x)$ with the average of those 10 curves (one for each τ). The behavior at each end of the curve, one for small x and one for x close to 1, is elucidated in Fig. 20.

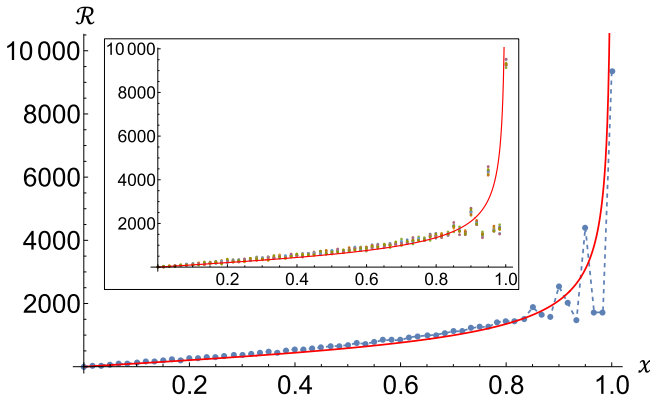


FIG. 19. Histograms representing the radial density of particles, as defined in this paper. Inset: Ten sets of dots, each with a unique color. Each set represents the average over ten simulations and corresponds to one unique value of τ from 17.0 to 17.9. Each set of dots represents the number of particles within a radial bin. There are 61 bins, i.e., 61 values of x ; $x = 0$ is the center of the cluster and $x = 1$ is at $r = R$. Fewer than ten dots appear at each x because some of the y values repeat. The solid curve is $\mathcal{R}(x)$ predicted by theory. The main plot contains only one set of dots, which is the average of all ten. The dots are connected by a dashed line to guide the eye to oscillations near $x = 1$. Simulations were done with $N = 1000$.

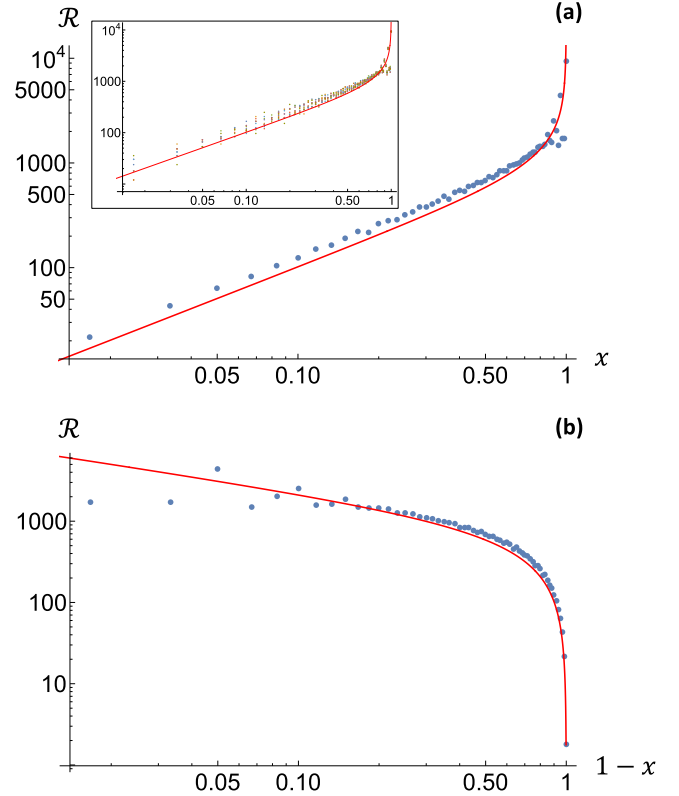


FIG. 20. (a) Same as Fig. 19, but on a log-log scale. (b) Same data as the main part of Fig. 19, but plotted vs $1 - x$ and on a log-log scale.

One obvious feature of simulation data (dots) in Fig. 19 is the oscillatory behavior close to $x = 1$. This happens because in a finite N system swarmalators organize themselves into rings; see, for instance, Fig. 3 or Fig. 5.

Whether this ring structure remains as N grows is not clear. Our theory, of course, assumes that at sufficiently large N continuum theory will work. In other words, there exists a continuum density $\rho(\mathbf{x})$, such that the number of swarmalators within a certain area ΔA that is much smaller than the area of the cluster is accurately given by $\rho(\mathbf{x})\Delta A$. This hypothesis is supported by our numerical observations (see, for example, Fig. 3) that the distance between swarmalators becomes smaller relative to the radius as N increases. The two panels in Fig. 20 demonstrate that theory matches numerical simulations quite well. We will now use the continuum theory to make predictions concerning the equilibrium radius and properties of breathing oscillations.

B. Key idea

The density profile $\tilde{\rho}$ was obtained by going to the $t \rightarrow \infty$ limit, when all motions cease. The system approaches this limit through decaying oscillations: $r_i(t) = r_i^* + \delta r_i(t)$, $R(t) = R^* + \delta R(t)$, and $\theta_i(t) = \Omega t + \delta \theta_i(t)$, where δr_i , $\delta R(t)$, and $\delta \theta_i(t)$ are decaying functions. We now introduce the key hypothesis: the profile $\tilde{\rho}$ holds not only at infinite time when oscillations have completely ceased, but even during the mature stages of these decaying oscillations. What this means

is that rearrangements of particles cease at these latter stages of the oscillations. We confirmed from simulations that this is indeed the case. Therefore, the density oscillates because the radius oscillates: the cluster overall expands and contracts, and particles get closer and further apart like on an expanding and contracting rubber sheet, while their relative positions and angles remains the same, and so the functional form of the density profile remains unchanging, i.e., $\tilde{\rho}$ holds true even during these latter stages of the decaying oscillations. With this key idea in mind, we can now derive coupled equations for the dynamics of θ_i , r_i , and R .

C. Reduced order model

As before, we will assume that all $\theta(t)$ are the same (modulo 2π). This is supported by simulation results; see Fig. 8 and Fig. 12, for example. Using the same procedure for passing into the continuum description as before (see discussion preceding Fig. 25), we have

$$\begin{aligned}\dot{\theta} &= \frac{K}{N} \sin[\theta(t - \tau) - \theta(t)] \sum_{j \neq i} \frac{1}{|\mathbf{r}_j(t) - \mathbf{r}_i(t)|} \\ &= \frac{2K}{N} \sin[\theta(t - \tau) - \theta(t)] \int_0^R r \rho(r, t) dr \\ &\quad \times \int_0^\pi \frac{d\alpha}{\sqrt{r^2 + l^2 - 2rl \cos \alpha}} \\ &= \frac{2K}{N} \sin[\theta(t - \tau) - \theta(t)] \int_0^R r \rho(r, t) \frac{2K \left[\frac{4lr}{(r+l)^2} \right]}{r+l} dr. \quad (9)\end{aligned}$$

We remind the reader that l is the radius position of i th swarmalator, i.e., it is a constant in our integrals, while r is the radius of j th swarmalators over which the summation (or integration, in continuum approximation) is performed. We now implement the key hypothesis and substitute $\rho(r, t) = \frac{5}{4} \frac{N}{\pi R^2(t)} \tilde{\rho}(r)$ and get

$$\begin{aligned}\dot{\theta} &= \frac{5K}{\pi R^2(t)} \sin[\theta(t - \tau) - \theta(t)] \int_0^{R(t)} r \tilde{\rho}(r) \frac{K \left[\frac{4lr}{(r+l)^2} \right]}{r+l} dr \\ &= \frac{5K}{\pi R(t)} \sin[\theta(t - \tau) - \theta(t)] \int_0^1 x \tilde{\rho}(x) \frac{K \left[\frac{4Lx}{(x+L)^2} \right]}{x+L} dx, \quad (10)\end{aligned}$$

where $L = l/R$ and $x = r/R$. But this is precisely the integral that defines $\tilde{\rho}$, and it evaluates to 1 [see Eq. 5]. Therefore, our equation becomes

$$\dot{\theta} = \frac{5K}{\pi R(t)} \sin[\theta(t - \tau) - \theta(t)]. \quad (11)$$

This is an interesting equation, but it is not closed, as we also need an equation for the $R(t)$. This closure will come from the spatial equation

$$\begin{aligned}\dot{\mathbf{r}}_i &= \frac{1}{N} \sum_{j \neq i} \left[\frac{\mathbf{r}_j - \mathbf{r}_i}{|\mathbf{r}_j - \mathbf{r}_i|} (1 + J \cos[\theta(t - \tau) - \theta(t)]) \right. \\ &\quad \left. - \frac{\mathbf{r}_j - \mathbf{r}_i}{|\mathbf{r}_j - \mathbf{r}_i|^2} \right]. \quad (12)\end{aligned}$$

The details of passing this into the continuum are provided in Appendix A 3. The crux of this analysis is the following equation:

$$\begin{aligned}\dot{l} &= \frac{5}{2\pi} \left[- (1 + J \cos[\theta(t - \tau) - \theta(t)]) \left(\frac{l}{R} \right) \right. \\ &\quad \left. + \frac{0.3\pi}{l} \left(\frac{4}{3} - \frac{2(2 + l/R)}{3} \sqrt{1 - l/R} \right) \right]. \quad (13)\end{aligned}$$

Three assumptions went into this result: (1) circular symmetry, (2) $\tilde{\rho}$ works even during the latter stages of decaying oscillations when particle rearrangements have ceased, and (3) all $\dot{\theta}_i$ are identical. All three assumptions are corroborated by simulations.

Equation (13) gives the instantaneous radial velocity of a particle located at distance l from the center. Setting $l = R$ gives the velocity of a particle on the edge, i.e., it gives \dot{R} . Thus, we finally arrive at two coupled equations for dynamics of R and θ [we reproduce here Eq. (11) for completeness]:

$$\dot{\theta} = \frac{5K}{\pi R(t)} \sin[\theta(t - \tau) - \theta(t)], \quad (14)$$

$$\dot{R} = \frac{5}{2\pi} \left[- (1 + J \cos[\theta(t - \tau) - \theta(t)]) + \frac{2\pi}{5R} \right]. \quad (15)$$

Equations (14) and (15) are two coupled equations for $\theta(t)$ and $R(t)$. We will study their dynamics soon, but, first, we analyze the $t \rightarrow \infty$ state, i.e., $R = R^*$, the constant value into which the radius settles, and $\theta = \Omega t$. These will be functions of J , K , and τ as we wanted. The following must be true in this static limit:

$$R^* = - \frac{5K}{\pi} \frac{\sin(\Omega\tau)}{\Omega}, \quad (16)$$

$$R^* = \frac{2\pi/5}{1 + J \cos(\Omega\tau)}. \quad (17)$$

We have already encountered the first of these; see Eq. (7). Combining the two, we get

$$1 + J \cos(\Omega\tau) = - \frac{2\pi^2}{25} \frac{\Omega/K}{\sin(\Omega\tau)}. \quad (18)$$

The solution $\Omega(\tau)$ is plotted in Fig. 21(a). The resulting $R^*(\tau)$, obtained through Eq. (16), is shown in Fig. 21(b). The obvious feature of these plots is the multivaluedness of solutions. At a certain critical value of τ , which we call τ_l , the Ω that solves Eq. (18) is zero. For $\tau > \tau_l$, there is nonzero Ω that satisfies Eq. (18). This is shown by the leftmost, black curves in Fig. 21. Eventually at τ somewhat above τ_l another solution appears. This is shown by the blue curves in Fig. 21: in fact, this family of roots comes in pairs. At a τ larger still, yet another family of roots appears, and so on. For $\tau < \tau_l$ a real solution to Eq. (18) does not exist. This means that Ω remains zero for $\tau < \tau_c$, a fact that can be verified by the numerical solution to Eqs. (14) and (15). In this case, the steady-state condition of Eq. (14) simply says $0 = 0$, and equilibrium radius is determined only from Eq. (15) [or from Eq. (17)], giving $R_l^* = \frac{2\pi/5}{1+J}$. The expression for τ_l can be obtained, for instance, by combining this result with Eq. (18) with $\Omega = 0$, giving $\tau_l = - \frac{2\pi^2}{25} \frac{1}{K(1+J)}$.

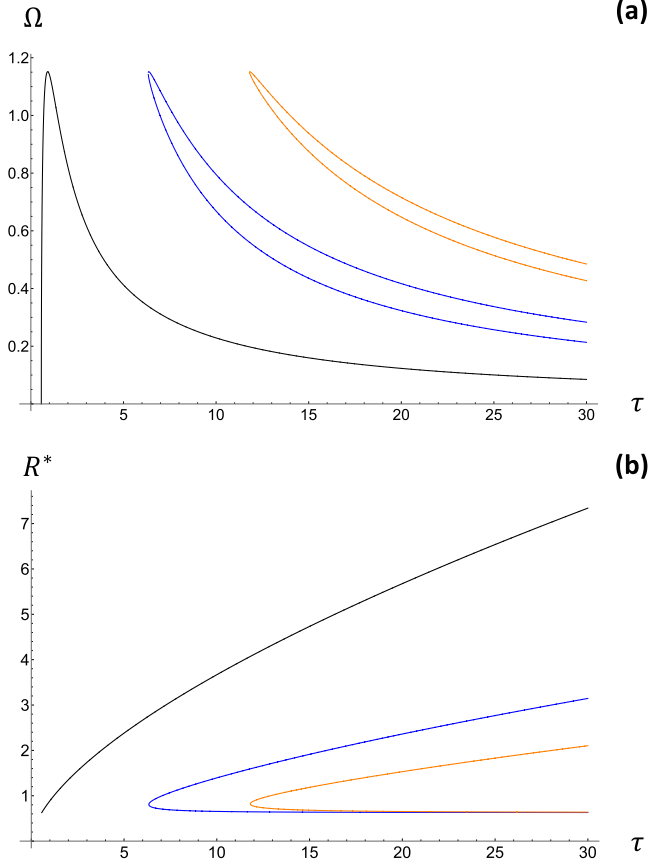


FIG. 21. (a) $\Omega(\tau)$; (b) $R^*(\tau)$. Multiple curves represent multiple solutions to Eqs. (16) and (17). The parameters are $J = 1$, $K = -0.7$.

Above τ_l , our continuum theory predicts a well-defined value of R^* . This is different from simulations, where R^* is only truly well defined above τ_c - which is greater than τ_l , although one can meaningfully talk about a time-averaged value of the radius of the cluster even below τ_c . Recall that τ_c denotes a transition between two types of long-time behaviors: from boiling to quasistatic pseudocrystal. On the other hand, a quantity such as τ_l in the context of the original model with $2N$ equations would represent a transition from synchronized swarmalators with a nonzero average $\dot{\theta}$ to unsynchronized with a zero average $\dot{\theta}$. The τ_l that we found is the estimate of this type of transition τ based on the assumptions that lead us to a two-equation approximation. On the other hand, the concept of τ_c does not exist in the continuum theory, because this theory is oblivious to surface fluctuations.

The shape of $R^*(\tau)$ in the first branch of Fig. 21 strongly resembles the shape of $R^*(\tau)$ obtained from simulations (see Fig. 9). We now would like to compare the two predictions. Note that the theoretical prediction is independent of N , while in presenting simulation results we observed the data collapse over different system sizes when instead of plotting R^* vs τ we plotted the dimensionless $(R^* - R_c^*)/R_c^*$ vs $(\tau - \tau_c)/\tau_c$. The equilibrium radius only truly makes sense above τ_c . This justifies why the rescaling had to be done with respect to τ_c , rather than τ_l . On the other hand, τ_c does not exist in the continuum theory, while the cluster radius is a function that is a constant ($\frac{2\pi/5}{1+J}$) below τ_l , and grows above τ_l . For this

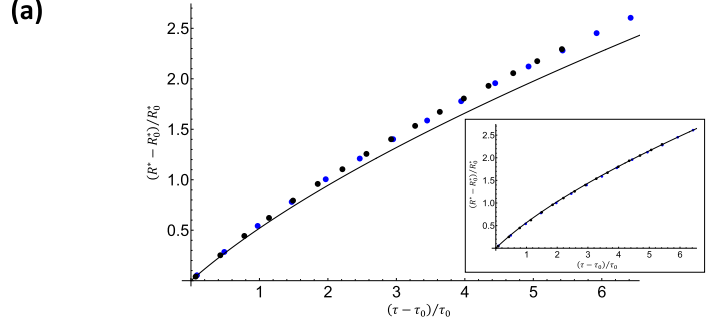


FIG. 22. Dots represent the simulation data [same data as in Fig. 9(b)]. Solid line is the theoretical prediction. Here τ_0 is τ_c for simulation results and $\tau_l = -\frac{2\pi^2}{25} \frac{1}{K(1+J)}$ for continuum theory. Similarly, R_0^* is R_c^* for simulation results and $R_l^* = \frac{2\pi/5}{1+J}$ for continuum theory. The difference between the two predictions disappears if the theoretical y values are multiplied by a factor ≈ 1.09 , as shown in the inset. The parameters are ($J = 1$, $K = -0.7$).

reason, we rescaled the x axis of the theoretical prediction by τ_l and the y axis by $(2\pi/5)/(1+J)$, and this was then compared with the dimensionless simulation data. This is shown in Fig. 22. While there is about a 9% difference between the predictions of the continuum theory with simulations, they in fact appear to match in functional form. This is seen in the inset of Fig. 22, where we multiplied the value of the analytical function by 1.09.

We now turn attention to relaxational dynamics of breathing oscillations predicted by Eqs. (14) and (15). Figure 23 depicts some examples of the evolution of θ and R in time. Solving these delayed equations numerically—as in solving the full dynamical equations—requires prehistory conditions. However, in contrast to the simulations

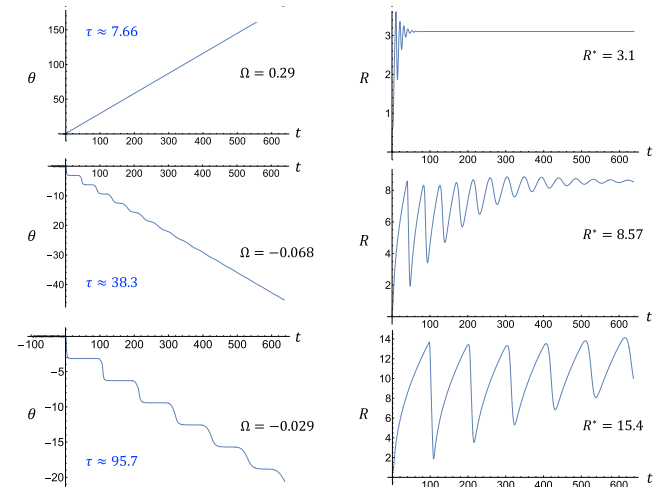


FIG. 23. Evolution of $\theta(t)$ and $R(t)$ with increasing τ , as predicted by the continuum theory. Here ($J = 1$, $K = -0.7$), which gives $\tau_l \approx 0.564$. The values of τ were chosen to be the same fraction of τ_l as in Fig. 32, which depicts simulation results (this assumes that τ_l in Fig. 32 is 1.65; see caption of that figure). The evaluation time (638) in these figures was chosen to be the same fraction of τ_l as in Fig. 32, $\approx 1131.3\tau_l$.

of dynamics from the full set of equations, here a constant initial condition would predict no evolution: $\theta(-\tau) - \theta(0) = 0$ results in $\dot{\theta} = 0$ and $\dot{R} = 0$ at $t = 0$. Our theory is meant to produce oscillations at large times, after rearrangements have ceased. Therefore, we chose prehistory that simulates complex, random-like behavior at earlier times (we see from simulations that early transient is complex). To this extent, we used the following prehistory for $-\tau < t < 0$: $\theta(t) = 0.01 \sum_{n=1}^{100} a_n \sin(nt - n^2)$, $R(t) = 0.01 \sum_{n=1}^{100} a_n \cos(nt - n^2)$, where a_n were a set of random numbers between 0 and 1. The phase offsets were used to eliminate spikes when t is an integer multiple of 2π . This is the type of prehistory that was used in producing Fig. 23.

The stepwise shape of $\theta(t)$ as well as the shape of $R(t)$ is qualitatively the same as simulations (see Fig. 32 below). We see that as τ increases, the period of decaying oscillations increases, and the decay rate decreases. These qualitative observations also match simulations. As time grows, both $\delta\theta(t)$ and $\delta R(t)$ evolve to a more pure harmonic, i.e., higher harmonics decay away quicker.

In presenting simulation results, we focused on the dynamical properties of long-time relaxations towards the equilibrium. There are only two: frequency and decay rate. To extract these from Eqs. (14) and (15) we linearize them by setting $\theta(t) = \Omega t + \delta\theta$ and $R(t) = R^* + \delta R$. The resulting linear equations for $\delta\theta$ and δR are

$$\frac{d}{dt}\delta\theta = [\delta\theta(t - \tau) - \delta\theta(t)] \left(\frac{5K \cos(\Omega\tau)}{\pi R^*} \right) + \delta R(t) \left(\frac{5K}{\pi (R^*)^2} \sin(\Omega\tau) \right), \quad (19)$$

$$\frac{d}{dt}\delta R = -\frac{5}{2\pi} J \sin(\Omega\tau) [\delta\theta(t - \tau) - \delta\theta(t)] - \frac{1}{(R^*)^2} \delta R. \quad (20)$$

Next, we seek solutions in the form

$$\begin{pmatrix} \delta\theta \\ \delta R \end{pmatrix} = \begin{pmatrix} \delta\theta_0 \\ \delta R_0 \end{pmatrix} e^{-\mu t}. \quad (21)$$

Substituting this ansatz into Eqs. (19) and (20) gives the following equation for eigenvalue μ :

$$\det \begin{pmatrix} (e^{\mu\tau} - 1) \left(\frac{5K \cos(\Omega\tau)}{\pi R^*} \right) + \mu & \frac{5K \sin(\Omega\tau)}{\pi (R^*)^2} \\ -(e^{\mu\tau} - 1) \left(\frac{5J}{2\pi} \sin(\Omega\tau) \right) & -\frac{1}{(R^*)^2} + \mu \end{pmatrix} = 0. \quad (22)$$

The solutions are generally complex. When we set $\mu = \lambda + i\omega$, substitute into the above equation, compute the determinant, and separate the real and imaginary parts, we get a pair of equations for two variables λ and ω . Each equation can be represented graphically as a zero contour of a function of two variables λ and ω . The solutions take place at the intersection of the two sets of contours. There is an infinite number of solutions, and we performed a numerical search for the solution with the lowest real part, which dominates at large times. For τ sufficiently close to τ_l the μ with the lowest real part is real and the motion becomes overdamped. Above such τ , the μ gains an imaginary part, and we get a complex conjugate pair of solutions.

In presenting dynamical properties of oscillations (for example, ω and λ) we observed that unlike the static properties, it was not necessary to perform rescaling of variables: the data for various N already collapse. This suggests that in comparing theory with simulations we will also not perform rescaling for the theoretical functions, such as $\lambda(\tau)$ or $\omega(\tau)$. With this idea in mind, we now compare these theoretical predictions with simulation results. This comparison is shown in Fig. 24. The theory (solid lines) predicts the scaling of both $\omega(\tau)$ and $\lambda(\tau)$ very well. In the case of ω s, it predicts the actual values, while there is an overall multiplicative factor of about 1.3 for decay rates.

Comparing between the predictions of the reduced-order theory and full simulations we see a very good match in the scaling of $\lambda(\tau)$ and $\Omega(\tau)$ at large τ . We remind the reader that it was not possible to obtain simulation results for sufficiently low τ , and the reason for this is explained at the end of Sec. III C. However, we can compare the values of τ_l , where phase synchronization first appears. The value of τ_l from the continuum theory is ≈ 0.564 for $(J = 1, K = -0.7)$. The value of τ_l from simulations for the same J and K was found to be between 1.6 and 1.7 for $N = 300$ and $N = 400$, and between 1.7 and 1.8 for $N = 100$. As τ is lowered significantly below τ_c , the thickness of the boiling layer grows (see Fig. 33). In this regime there is a strong variation of velocity vectors between even nearest-neighbor particles. Therefore, we expect the continuum theory to break down for τ significantly below τ_c . Notice that there is still a good match below, but close to, τ_c .

V. DISCUSSION AND SUMMARY

We presented a study on the role of time delay in interacting swarmalators, although a recent work has studied delays in Vicsek-type models [55]. Two long-time collective states due to delay were discovered. In the first state, swarmalators settle into a quasistatic cluster in a pseudocrystalline arrangement.

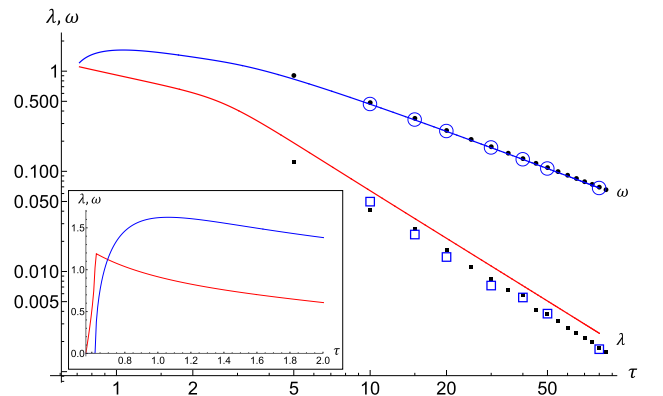


FIG. 24. The numerical data (squares and circles) are exactly the same as in Fig. 17. The solid lines are theoretical predictions: decay rate λ (lower, red) and angular frequency ω (upper, blue). Inset: Theoretical λ and ω at low $\tau > \tau_l$, plotted on a linear scale. The transition to overdamped solutions, where eigenvalues are purely real (i.e., $\omega = 0$) is clearly seen at $\tau \approx 0.62$. The values of τ_c are 10.11 ± 0.24 for $N = 300$ (blue open symbols) and 14.03 ± 0.4 (black solid symbols).

It is quasistatic because particles execute creeping motions with very small velocities. In the second state that happens at lower values of time delay, the swarmalators close to the surface perform boiling-like convective motions. The transient that leads into both of these states has an early-time component and a much longer stage that involves collective oscillations of the whole cluster, which give the cluster the breathing-like effect. Throughout most of this longer phase of the transient particles have already finished rearrangements, and internal phases of swarmalators have already synchronized. We have not thoroughly mapped the (J, K) parameter space, so other collective phenomena caused by the delay are possible.

We also proposed a phenomenological continuum theory, based on the idea that particle rearrangements complete at fairly early times, so particles have settled into fixed relative positions during the latter stages of breathing oscillations. Therefore, the infinite time equilibrium density profile, which we were able to calculate using this continuum theory, also holds throughout these latter stages of the breathing. This allowed us to calculate frequency and decay rates of breathing, which match numerical results well. This ansatz is confirmed with simulations, but it would need to be put on a firmer theoretical understanding in future work. The other two assumptions are circular symmetry and phase synchronization at early stages of the breathing. The existence of early phase synchronization especially also needs to be understood more fully in the future. However, all three assumptions are corroborated with numerical simulations. While the phase slips appear to take place simultaneously for all swarmalators, there are tiny differences in which particles experience the slips first. It would also be interesting to understand if there is a relationship between local structural properties and dynamics of phase slips. Finally, the creeping motion in the quasistatic pseudocrystal reminds us of glassy phenomena. Exploring the role of frustration and aging on swarmalator phenomena would be a tantalizing avenue of future research.

An earlier version of this work was a part of an undergraduate senior project by one of the coauthors, Nicholas Blum [56]. Some of the figures from this senior project are reproduced here.

ACKNOWLEDGMENTS

We would like to thank Evgeniy Khain for a useful discussion. A part of this work was done with the financial support from William and Linda Frost fund for undergraduate summer research at Cal Poly.

APPENDIX A: CALCULATIONAL DETAILS

1. Passing of Eq. (3) into the continuum

Consider two swarmalators: swarmalator i , located at radius l , and swarmalator j , located at radius r and angle α . Because of radial symmetry, the sum will not depend on the angle of swarmalator i , so it is convenient to place it at zero angle relative to an arbitrary x axis. The situation is illustrated in the schematic in Fig. 25. With such a setup, and the use of the density $\rho(r)$, the sum in Eq. (3), which we will call s here,

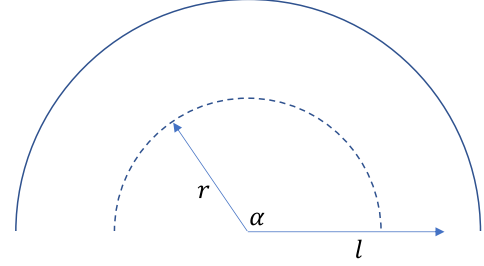


FIG. 25. Geometry for evaluating Eq. (3).

becomes

$$s = 2 \int_0^R dr \int_0^\pi \frac{\rho(r)r d\alpha}{\sqrt{r^2 + l^2 - 2rl \cos \alpha}}. \quad (\text{A1})$$

We also depict the K discussed below Eq. (4) in Fig. 26.

2. Comment concerning the radial probability density $\mathcal{R}(x)$

Since $r = xR$, it might at first seem that a factor R is missing from the denominator in the expression of $\mathcal{R}(x) = \frac{5}{2}Nx\tilde{\rho}(x)$. But, in fact, it is this form that normalizes to N . In other words,

$$\begin{aligned} \int_0^1 \mathcal{R}(x) dx &= \frac{5}{2}N \int_0^R \frac{r}{R} \tilde{\rho}(r) \frac{dr}{R} \\ &= \frac{5}{2} \frac{N}{R^2} \int_0^R r \tilde{\rho}(r) dr \\ &= \frac{5}{4} \frac{N}{\pi R^2} \int_0^R 2\pi r \tilde{\rho}(r) dr \\ &= \int_0^R 2\pi r \rho(r) dr = N. \end{aligned}$$

We used Eq. (8) in going from $\tilde{\rho}(r)$ to $\rho(r)$. Thus, $\frac{dr}{R}$ in the integration measure is what required the correct definition of $\mathcal{R}(x)$ not to have the R in the denominator. In doing the analysis of data, we also normalize the histogram binned by radii, so that $\sum_i \mathcal{R}_i \Delta x = N$.

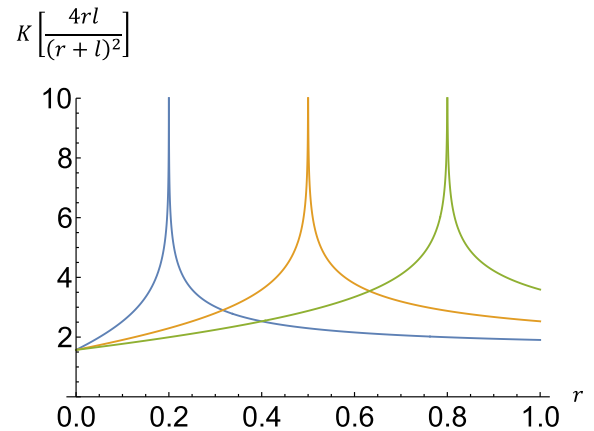


FIG. 26. $K \left[\frac{4rl}{(r+l)^2} \right]$ as a function of r for $l = 0.2$ (left, blue), 0.5 (middle, orange), and 0.8 (right, green).

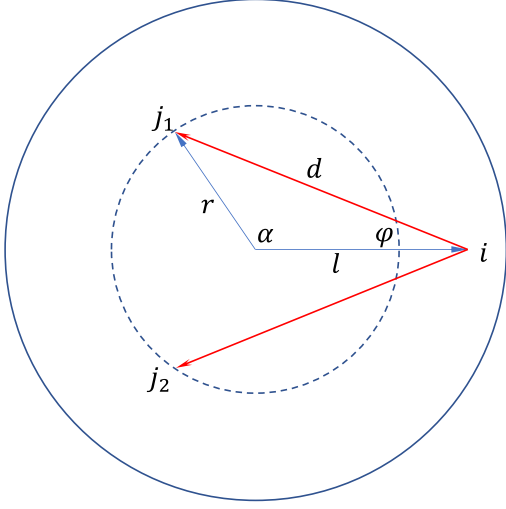


FIG. 27. Geometry for evaluating Eq. (A2).

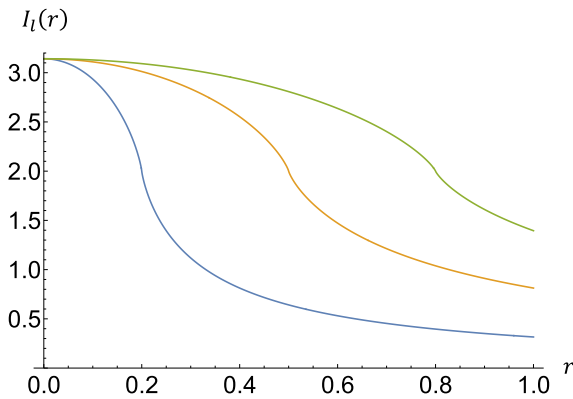
3. Passing Eq. (A2) into the continuum

The starting point is the spatial equation

$$\dot{\mathbf{r}}_i = \frac{1}{N} \sum_{j \neq i}^N \left[\frac{\mathbf{r}_j - \mathbf{r}_i}{|\mathbf{r}_j - \mathbf{r}_i|} (1 + J \cos [\theta(t - \tau) - \theta(t)]) - \frac{\mathbf{r}_j - \mathbf{r}_i}{|\mathbf{r}_j - \mathbf{r}_i|^2} \right]. \quad (\text{A2})$$

We are going to assume that all phases synchronize. Consider the first term. Here we are adding unit vectors pointing from the i th particle to all other particles. Because of circular symmetry, for each particle above, there is another symmetric partner on the opposite side; see Fig. 27.

Thus, for each i th particle, all vectors will point towards the center of the cluster. Going into the continuum limit, the


 FIG. 28. $I_l(r)$ for $l = 0.2$ (bottom, blue), 0.5 (middle, orange) and 0.8 (top, green).

first sum becomes

$$- [2(1 + J \cos [\theta(t - \tau) - \theta(t)])] \int_0^R r \rho(r) dr \times \int_0^\pi \cos [\varphi(\alpha)] d\alpha \hat{\mathbf{R}}. \quad (\text{A3})$$

We can find $\cos [\varphi(\alpha)]$ using a combination of laws of sines and cosines. From the law of sines we have $\sin \varphi = \frac{r \sin \alpha}{d}$, so $1 - \cos^2 \varphi = \frac{r^2 \sin^2 \alpha}{d^2}$. Thus $\cos [\varphi(\alpha)] = \sqrt{1 - \frac{r^2 \sin^2 \alpha}{d^2}} = \frac{l - r \cos \alpha}{\sqrt{r^2 + l^2 - 2rl \cos \alpha}}$. From this, the inner integral over α is $\int_0^\pi \frac{l - r \cos \alpha}{\sqrt{r^2 + l^2 - 2rl \cos \alpha}} d\alpha$. This integral can be evaluated as

$$I_l(r) = \int_0^\pi \frac{l - r \cos \alpha}{\sqrt{r^2 + l^2 - 2rl \cos \alpha}} d\alpha = \left| \frac{(r-l)}{l} E \left[-\frac{4rl}{(r-l)^2} \right] - \frac{(r+l)}{l} K \left[-\frac{4rl}{(r-l)^2} \right] \right|, \quad (\text{A4})$$

where E is a complete elliptic integral of the second kind. We plot $I_l(r)$ for several l in Fig. 28. Note that although $I_l(r)$ quantity is not defined at $r = l$, the limit of $r \rightarrow l$ from both sides exists and equals 2. Thus, the first term in Eq. (A2) equals

$$- \left[2(1 + J \cos [\theta(t - \tau) - \theta(t)]) \int_0^R r \rho(r) \times \left| \frac{(r-l)}{l} E \left[-\frac{4rl}{(r-l)^2} \right] - \frac{(r+l)}{l} K \left[-\frac{4rl}{(r-l)^2} \right] \right| dr \right] \hat{\mathbf{R}}.$$

We now turn our attention to the second term. The inner integral in this term would be $2 \int_0^\pi \frac{l - r \cos \alpha}{r^2 + l^2 - 2rl \cos \alpha} d\alpha$. It evaluates to $2\pi/l$ when $r < l$ and 0 when $r > l$. In the second case, the repulsive force from particles “to the right” of the i th particle and the repulsive force from particles “to the left” of the i th particle add up to zero (see Fig. 27). This is similar to the electric (or gravitational) field inside a hollow shell. A particle inside a shell of charge (or mass) experiences no net force. But a particle outside a sphere of charge (or mass) does experience a net force. So the second term in the spatial equation becomes $[\frac{2\pi}{l} \int_0^l r \rho(r) dr] \hat{\mathbf{R}}$. All together, the spatial equation gives

$$\dot{\mathbf{i}} = \frac{1}{N} \left[-2(1 + J \cos [\theta(t - \tau) - \theta(t)]) \int_0^R r \rho(r) \times \left| \frac{(r-l)}{l} E \left[-\frac{4rl}{(r-l)^2} \right] - \frac{(r+l)}{l} K \left[-\frac{4rl}{(r-l)^2} \right] \right| dr + \frac{2\pi}{l} \int_0^l r \rho(r) dr \right], \quad (\text{A5})$$

and no dynamics in the angular direction. Particle motion is purely in the radial direction due to the circular symmetry. This can be expected to be true only in the continuum limit; in the discrete case, there might not be an exact cancellation of the two vectors (in Fig. 27), which would allow for some angular motion. We now substitute for $\rho(r) = \frac{5}{4} \frac{N}{\pi R^2} \tilde{\rho}(r)$ [see Eq. (8)], using $\tilde{\rho} = 0.3(1 - r/R)^{-1/2}$, which, as we saw, is a good model of the numerical solution. The first integral cannot be expressed in terms of elementary functions, but it

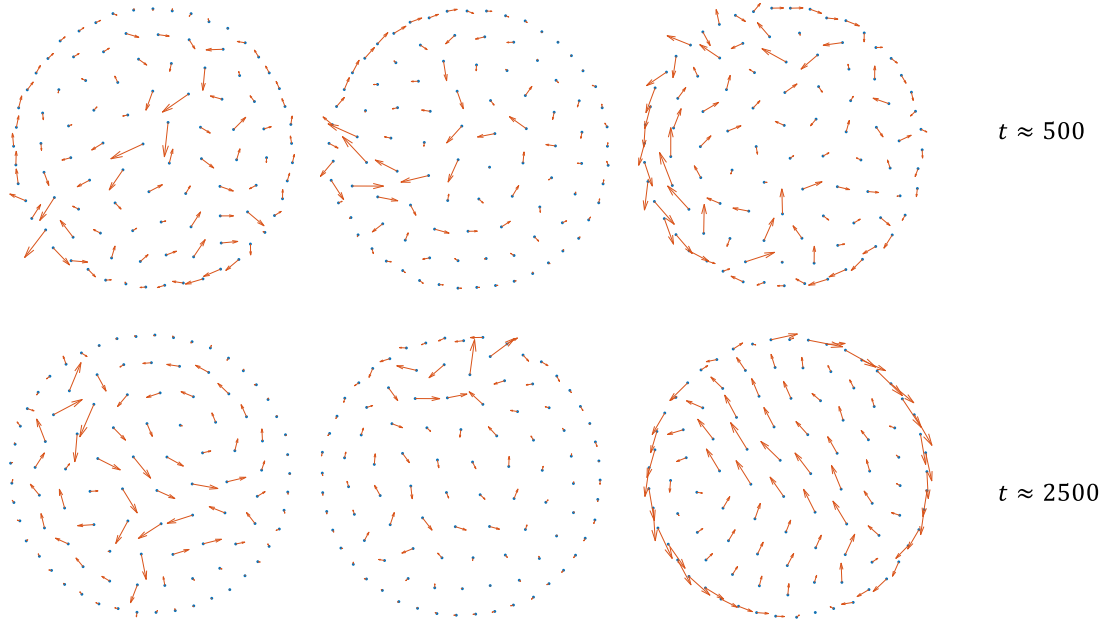


FIG. 29. Examples of creeping motion for $N = 100$. In all examples, breathing ended between $t = 250$ and $t = 300$. Here $\tau = 1.5\tau_c$ with $J = 1$ and $K = -0.7$.

is very closely approximated by $\frac{5}{4}\frac{N}{\pi}\frac{l}{R}$. The second integral evaluates to $\frac{5}{4}\frac{N}{\pi} \times 0.3\left(\frac{4}{3} - \frac{2(2+l/R)}{3}\sqrt{1-l/R}\right)$. Therefore,

$$\dot{i} = \frac{5}{2\pi} \left[- (1 + J \cos[\theta(t - \tau) - \theta(t)]) \left(\frac{l}{R}\right) + \frac{0.3\pi}{l} \left(\frac{4}{3} - \frac{2(2+l/R)}{3}\sqrt{1-l/R}\right) \right]. \quad (\text{A6})$$

APPENDIX B: ADDITIONAL PLOTS

Figures 29 and 30 provide more examples of the creeping motion that takes place after the breathing transient. Figure 29 is for $N = 100$, and Fig. 30 is for $N = 400$. The lengths of arrows that represent particle velocity vectors have been up-scaled to be visible; of course, these velocities are very small in comparison to velocities during the breathing stage. We see that in some cases the velocity patterns are localized,

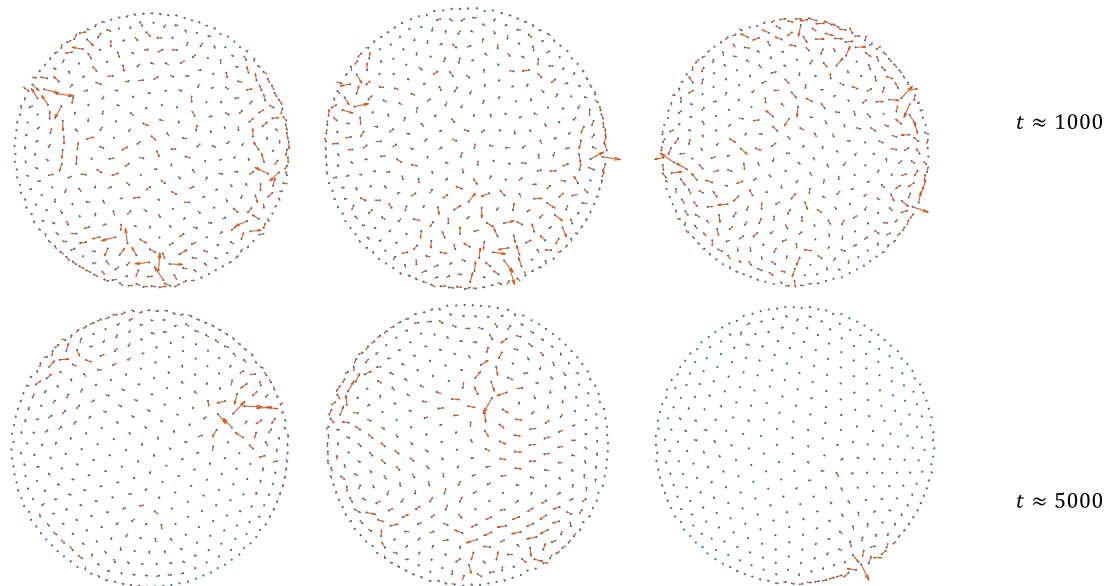


FIG. 30. Examples of creeping motion for $N = 400$. In all examples, breathing ended between $t = 500$ and $t = 600$. Here $\tau = 1.5\tau_c$ with $J = 1$ and $K = -0.7$.

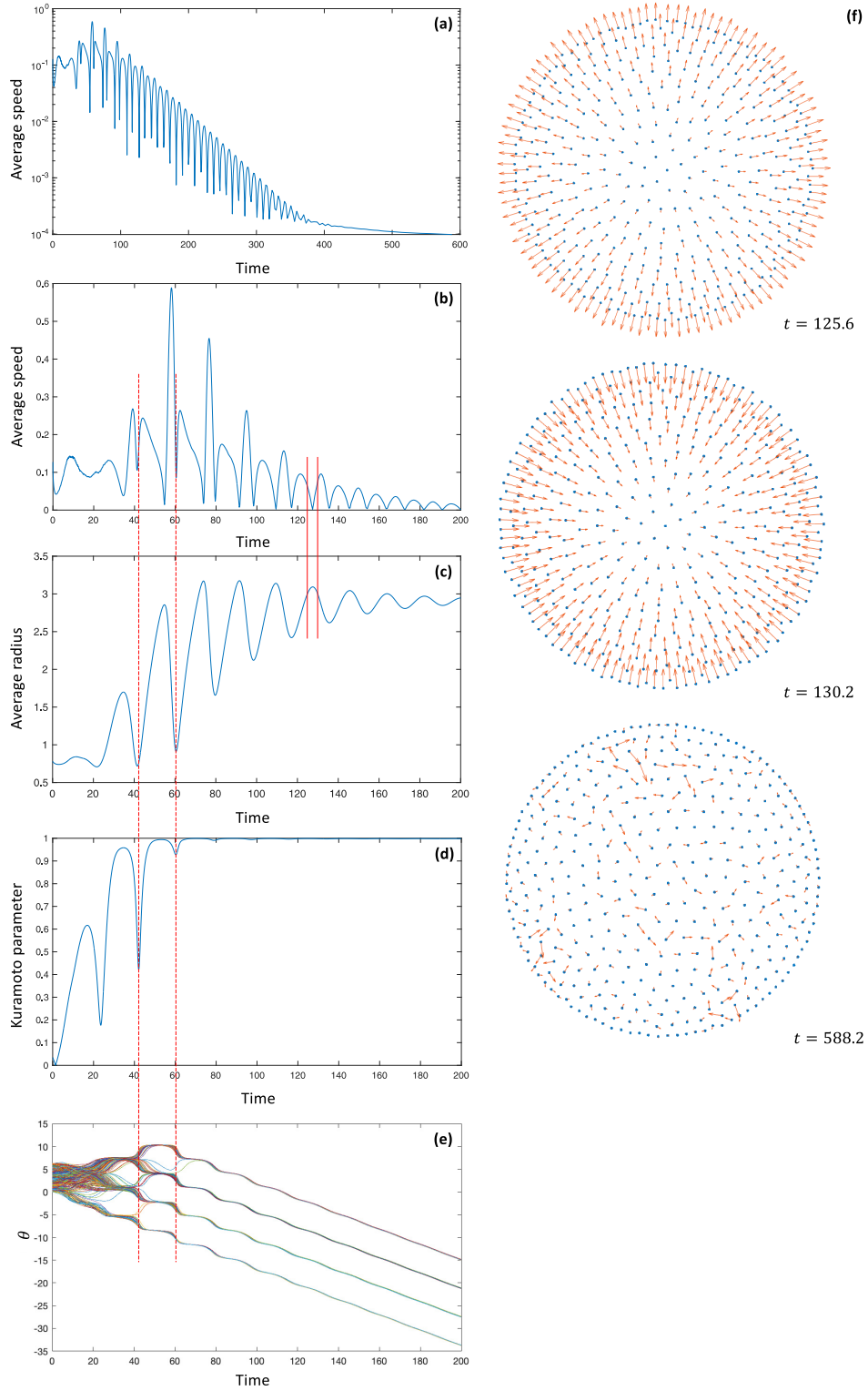


FIG. 31. (a) $|\bar{v}|(t)$ on a logarithmic scale. (b) $|\bar{v}|(t)$ on a linear scale and in a shorter time window that shows only the early transient, the onset of breathing, and breathing in their latter stages. (c) $\bar{R}(t)$. (d) Kuramoto order parameter. (e) $\theta(t)$ for each swarmalator. (f) Snapshots of particle positions and velocity vectors at three instants of time. Here $J = 1$, $K = -0.7$, $N = 400$, $\tau = 1.3\tau_c$.

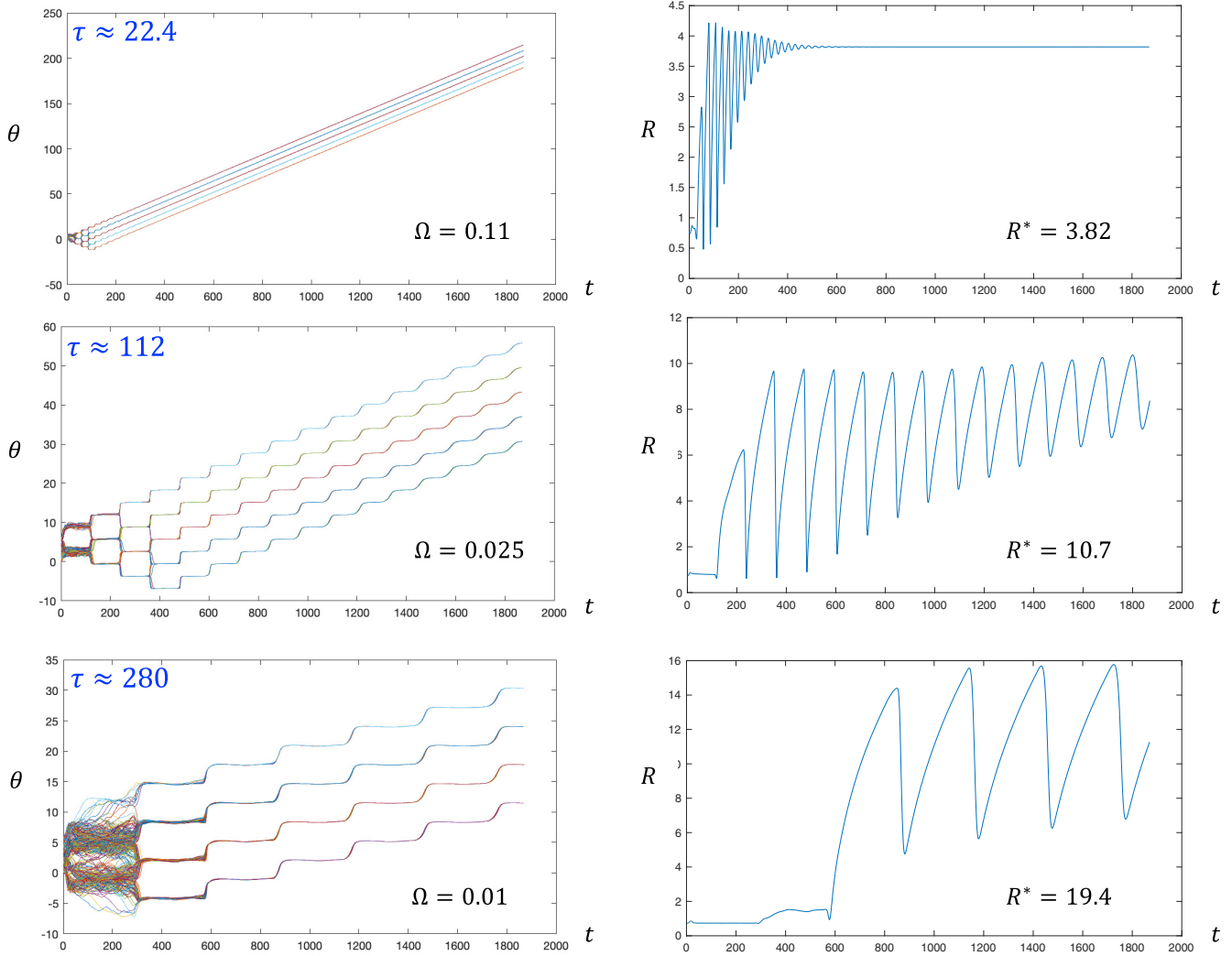


FIG. 32. Evolution of $\theta(t)$ and $R(t)$ with increasing τ , as predicted by the simulations. Here $K = -0.7$ and $N = 400$. For this (N, K) , $\tau_c = 11.2 \pm 0.26$, so the first graph is at $\tau = 2\tau_c$. The value of τ_l is between 1.6 and 1.7.

but not always. It may be that localization is more common at later times and occurs near the edge, but we have not done a systematic study to conclude this definitively.

Next, we present an example of the dynamics for τ above τ_c in Fig. 31. The two long vertical red lines are placed at two subsequent dips in the Kuramoto order parameter. These dips happen at the time when the phases slip. When this happens, there is a window of time when the phases of swarmsalators are not all the same, before they all resynchronize. The details

of this process can be a subject of study in the future. We also show several patterns: two during the late stages of breathing [we placed two short red lines in $\bar{v}(t)$ and $R(t)$ graphs at approximately these instants of time] and one postbreathing. The next plot, in Fig. 32, demonstrates how the dynamics as predicted by simulations evolves with τ .

The last plot, Fig. 33, demonstrates how the long-time behavior that takes place after breathing oscillations evolves with τ , as it is lowered from above to below τ_c .

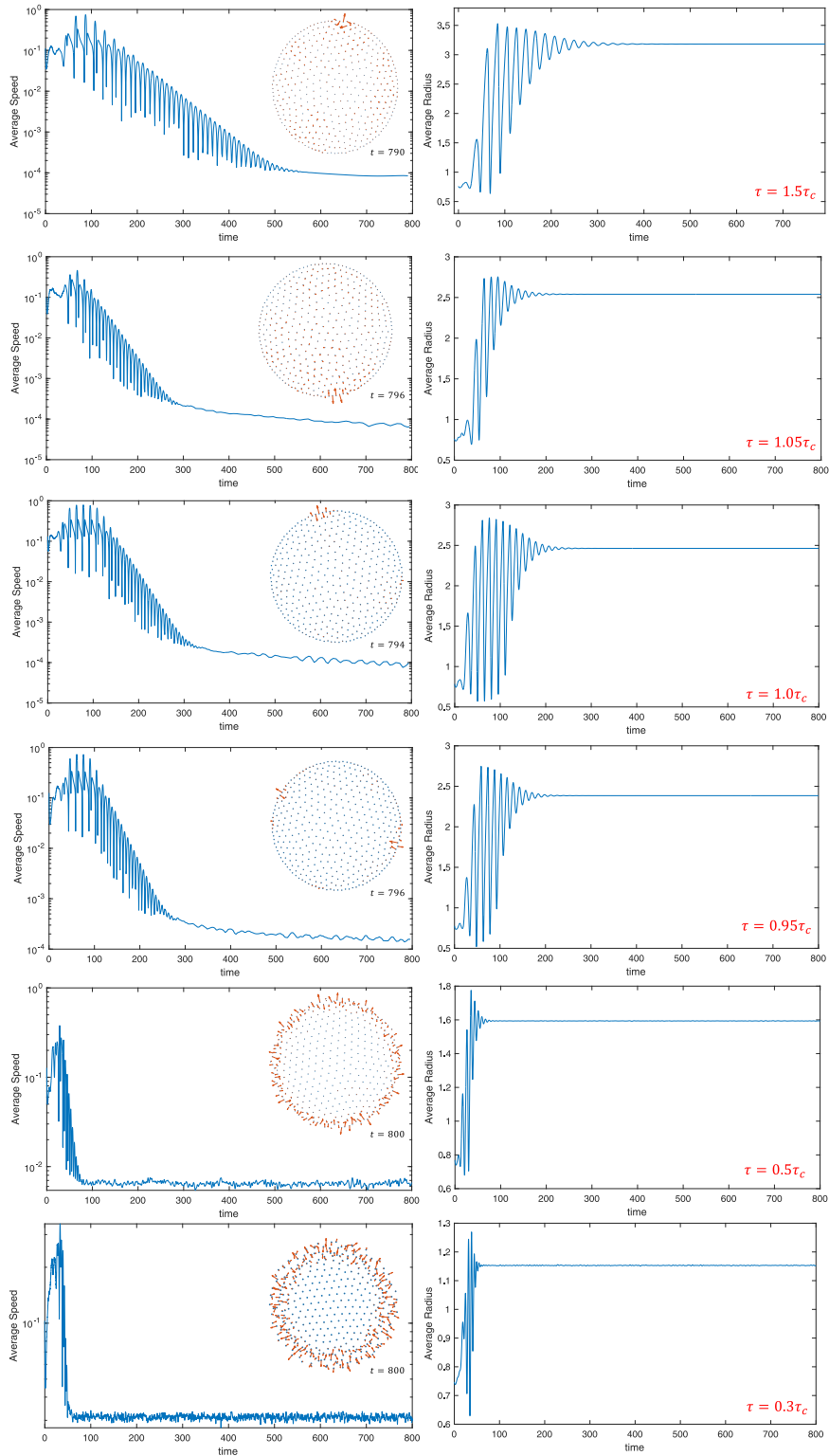


FIG. 33. Evolution of particle dynamics with decreasing τ . The boiling surface appears around τ_c , and its width grows as τ is progressively decreased. Clusters for τ below τ_l are not shown. Here $N = 400$, $J = 1$, $K = -0.7$.

- [1] K. P. O'Keeffe, H. Hong, and S. H. Strogatz, *Nat. Commun.* **8**, 1504 (2017).
- [2] Y. Yang, J. Elgeti, and G. Gompper, *Phys. Rev. E* **78**, 061903 (2008).
- [3] I. H. Riedel, K. Kruse, and J. Howard, *Science* **309**, 300 (2005).
- [4] A. C. Quillen, A. Peshkov, E. Wright, and S. McGaffigan, *Phys. Rev. E* **104**, 014412 (2021).
- [5] A. Peshkov, S. McGaffigan, and A. C. Quillen, *Soft Matter* **18**, 1174 (2022).
- [6] S. L. Tamm, T. Sonneborn, and R. V. Dippell, *J. Cell Biol.* **64**, 98 (1975).
- [7] B. Verberck, *Nat. Phys.* **18**, 131 (2022).
- [8] M. Belovs, R. Livanovičs, and A. Cēbers, *Phys. Rev. E* **96**, 042408 (2017).
- [9] J. Yan, M. Bloom, S. C. Bae, E. Luijten, and S. Granick, *Nature (London)* **491**, 578 (2012).
- [10] S. Hwang, T. D. Nguyen, S. Bhaskar, J. Yoon, M. Klaiber, K. J. Lee, S. C. Glotzer, and J. Lahann, *Adv. Funct. Mater.* **30**, 1907865 (2020).
- [11] B. Zhang, A. Sokolov, and A. Snezhko, *Nat. Commun.* **11**, 4401 (2020).
- [12] A. Bricard, J.-B. Caussin, D. Das, C. Savoie, V. Chikkadi, K. Shitara, O. Chepizhko, F. Peruani, D. Saintillan, and D. Bartolo, *Nat. Commun.* **6**, 7470 (2015).
- [13] B. Zhang, H. Karani, P. M. Vlahovska, and A. Snezhko, *Soft Matter* **17**, 4818 (2021).
- [14] R. K. Manna, O. E. Shklyaev, and A. C. Balazs, *Proc. Natl. Acad. Sci. USA* **118**, e2022987118 (2021).
- [15] M. Li, M. Brinkmann, I. Pagonabarraga, R. Seemann, and J.-B. Fleury, *Commun. Phys.* **1**, 23 (2018).
- [16] K. Chaudhary, J. J. Juárez, Q. Chen, S. Granick, and J. A. Lewis, *Soft Matter* **10**, 1320 (2014).
- [17] A. Hrabec, V. Křižáková, S. Pizzini, J. Sampaio, A. Thiaville, S. Rohart, and J. Vogel, *Phys. Rev. Lett.* **120**, 227204 (2018).
- [18] E. Haltz, S. Krishnia, L. Berges, A. Mougin, and J. Sampaio, *Phys. Rev. B* **103**, 014444 (2021).
- [19] A. Barciś, M. Barciś, and C. Bettstetter, in *2019 International Symposium on Multi-Robot and Multi-Agent Systems (MRS)* (IEEE, New York, 2019), pp. 98–104.
- [20] A. Barciś and C. Bettstetter, *IEEE Access* **8**, 218752 (2020).
- [21] U. Schilcher, J. F. Schmidt, A. Vogell, and C. Bettstetter, in *2021 IEEE International Conference on Autonomic Computing and Self-Organizing Systems (ACSOS)* (IEEE, New York, 2021), pp. 90–99.
- [22] J. D. Monaco, G. M. Hwang, K. M. Schultz, and K. Zhang, *Biol. Cybern.* **114**, 269 (2020).
- [23] A. Hadzic, G. M. Hwang, K. Zhang, K. M. Schultz, and J. D. Monaco, *Array* **15**, 100218 (2022).
- [24] B. Rinner, C. Bettstetter, H. Hellwagner, and S. Weiss, *Computer* **54**, 34 (2021).
- [25] G. Gardi, S. Ceron, W. Wang, K. Petersen, and M. Sitti, *Nat. Commun.* **13**, 2239 (2022).
- [26] Y. Origane and D. Kurabayashi, *Symmetry* **14**, 1578 (2022).
- [27] T. H. Tan, A. Mietke, H. Higinbotham, J. Li, Y. Chen, P. J. Foster, S. Gokhale, J. Dunkel, and N. Fakhri, *Nature* **607**, 287 (2022).
- [28] G. Petrunaro, L. G. Morelli, and K. Uriu, *Semi. Cell & Develop. Bio.* **93**, 26 (2019).
- [29] D. Tanaka, *Phys. Rev. Lett.* **99**, 134103 (2007).
- [30] M. Iwasa, K. Iida, and D. Tanaka, *Phys. Rev. E* **81**, 046220 (2010).
- [31] M. Iwasa, K. Iida, and D. Tanaka, *Phys. Lett. A* **376**, 2117 (2012).
- [32] M. Iwasa and D. Tanaka, *Phys. Lett. A* **381**, 3054 (2017).
- [33] H. Hong, *Chaos* **28**, 103112 (2018).
- [34] H. K. Lee, K. Yeo, and H. Hong, *Chaos* **31**, 033134 (2021).
- [35] F. Jiménez-Morales, *Phys. Rev. E* **101**, 062202 (2020).
- [36] P. Japón, F. Jiménez-Morales, and F. Casares, *Cells Develop.* **169**, 203726 (2022).
- [37] J. U. Lizarraga and M. A. de Aguiar, *Chaos* **30**, 053112 (2020).
- [38] K. O'Keeffe, S. Ceron, and K. Petersen, *Phys. Rev. E* **105**, 014211 (2022).
- [39] S. Yoon, K. P. O'Keeffe, J. F. F. Mendes, and A. V. Goltsev, *Phys. Rev. Lett.* **129**, 208002 (2022).
- [40] K. O'Keeffe and H. Hong, *Phys. Rev. E* **105**, 064208 (2022).
- [41] G. K. Sar, D. Ghosh, and K. O'Keeffe, *Phys. Rev. E* **107**, 024215 (2023).
- [42] T. A. McLennan-Smith, D. O. Roberts, and H. S. Sidhu, *Phys. Rev. E* **102**, 032607 (2020).
- [43] H. Hong, K. Yeo, and H. K. Lee, *Phys. Rev. E* **104**, 044214 (2021).
- [44] G. K. Sar, S. N. Chowdhury, M. Perc, and D. Ghosh, *New J. Phys.* **24**, 043004 (2022).
- [45] K. P. O'Keeffe, J. H. M. Evers, and T. Kolokolnikov, *Phys. Rev. E* **98**, 022203 (2018).
- [46] S.-Y. Ha, J. Jung, J. Kim, J. Park, and X. Zhang, *Kinetic Related Models* **14**, 429 (2021).
- [47] S.-Y. Ha, J. Jung, J. Kim, J. Park, and X. Zhang, *Math. Models Methods Appl. Sci.* **29**, 2225 (2019).
- [48] P. Degond, A. Diez, and A. Walczak, *Anal. Appl.* **20**, 1215 (2022).
- [49] G. K. Sar and D. Ghosh, *Europhys. Lett.* **139**, 53001 (2022).
- [50] K. O'Keeffe and C. Bettstetter, in *Micro- and Nanotechnology Sensors, Systems, and Applications XI*, edited by T. George and M. S. Islam, Vol. 10982 (SPIE, Philadelphia, 2019), p. 109822E.
- [51] N. Fujiwara, J. Kurths, and A. Díaz-Guilera, *Phys. Rev. E* **83**, 025101(R) (2011).
- [52] K. Uriu, S. Ares, A. C. Oates, and L. G. Morelli, *Phys. Rev. E* **87**, 032911 (2013).
- [53] D. Levis, I. Pagonabarraga, and A. Díaz-Guilera, *Phys. Rev. X* **7**, 011028 (2017).
- [54] S. Majhi, D. Ghosh, and J. Kurths, *Phys. Rev. E* **99**, 012308 (2019).
- [55] Y. Sun, W. Li, L. Li, G. Wen, S. Azaele, and W. Lin, *Phys. Rev. Res.* **4**, 033054 (2022).
- [56] N. S. Blum, Digital Commons @ Calpoly (2021), <https://digitalcommons.calpoly.edu/physpp/205/>.